Chemical Geology 388 (2014) 23–39

Contents lists available at ScienceDirect

Chemical Geology

journal homepage: www.elsevier.com/locate/chemgeo

Origin and interactions of fluids circulating over the Amik Basin (Hatay, Turkey) and relationships with the hydrologic, geologic and tectonic settings

G. Yuce [a], F. Italiano [b], W. D'Alessandro [b,*], T.H. Yalcin [c], D.U. Yasin [d], A.H. Gulbay [d], N.N. Ozyurt [a], B. Rojay [e], V. Karabacak [d], S. Bellomo [b], L. Brusca [b], T. Yang [f], C.C. Fu [g], C.W. Lai [f], A. Ozacar [e], V. Walia [h]

[a] Hacettepe University, Department of Geological Engineering, Hydrogeology Division, Beytepe, 06800 Ankara, Turkey
[b] Istituto Nazionale di Geofisica e Vulcanologia, Sezione di Palermo, Via Ugo La Malfa, 153, 90146 Palermo, Italy
[c] Istanbul Technical University, Faculty of Mining, Department of Geological Engineering, Maslak, 34469 Istanbul, Turkey
[d] Eskisehir Osmangazi University, Department of Geological Engineering, Meselik, 26480 Eskisehir, Turkey
[e] Middle East Technical University, Department of Geological Engineering, 06531 Ankara, Turkey
[f] National Taiwan University, Department of Geosciences, Roosevelt Road, Taipei 106, Taiwan
[g] Institute of Earth Sciences of Academia Sinica, Taiwan
[h] National Center for Research on Earthquake Engineering (NCREE), 200, Sec. 3, Xinhai Road, Taipei 106, Taiwan

ARTICLE INFO

Article history:
Received 28 May 2014
Received in revised form 28 August 2014
Accepted 2 September 2014
Available online 16 September 2014

Editor: David R. Hilton

Keywords:
Dead Sea Fault
Hydrogeochemistry
Gas geochemistry
He isotopes
C isotopes
Ophiolites

ABSTRACT

We investigated the geochemical features of the fluids circulating over the Amik Basin (SE Turkey–Syria border), which is crossed by the Northern extension of the DSF (Dead Sea Fault) and represents the boundary area of three tectonic plates (Anatolian, Arabian and African plates). We collected 34 water samples (thermal and cold from natural springs and boreholes) as well as 8 gas samples (bubbling and gas seepage) besides the gases dissolved in the sampled waters. The results show that the dissolved gas phase is a mixture of shallow (atmospheric) and deep components either of mantle and crustal origin. Coherently the sampled waters are variable mixtures of shallow and deep ground waters, the latter being characterised by higher salinity and longer residence times. The deep groundwaters (from boreholes deeper than 1000 m) have a CH_4-dominated dissolved gas phase related to the presence of hydrocarbon reservoirs. The very unique tectonic setting of the area includes the presence of an ophiolitic block outcropping in the westernmost area on the African Plate, as well as basalts located to the North and East on the Arabic Plate.

The diffuse presence of CO_2-enriched gases, although diluted by the huge groundwater circulation, testifies a regional degassing activity. Fluids circulating over the ophiolitic block are marked by H_2-dominated gases with abiogenic methane and high-pH waters. The measured $^3He/^4He$ isotopic ratios display contributions from both crustal and mantle-derived sources over both sides of the DSF. Although the serpentinization process is generally independent from mantle-type contribution, the recorded helium isotopic ratios highlight variable contents of mantle-derived fluids. Due to the absence of recent volcanism over the western side of the basin (African Plate), we argue that CO_2-rich volatiles carrying mantle-type helium and enriched in heavy carbon, are degassed by deep-rooted regional faults rather than from volcanic sources.

1. Introduction

The Amik Basin is the intersection domain of several active, regional-scale structural lineaments (Fig. 1), namely the N trending sinistral Dead Sea Fault (DSF), the NE trending sinistral East Anatolian Fault (EAF) and the NE trending contractional Cyprus Arc (CA). These three regional scale tectonic structures represent the margin of the Anatolian, Arabian and African plates (Mahmoud et al., 2013). Such complex geological setting is reflected in the outcropping of a large variety of rock units.

The Amik Basin is a well-recognised depression bounded by elevated shoulders. It is the widest and deepest part of the Karasu rift, and its main depocenter (Fig. 2). The eastern and western margins of the rift display morphological differences: the western margin (the Amanos Mountains) is uplifted to a height of up to 2250 m, while the eastern margin has a relatively low topography up to 800 m asl as a consequence of the asymmetric evolution of the basin.

The DSF is a seismically active tectonic structure crossing Israel, Jordan, Syria and Turkey following a nearly N–S direction (e.g. Quennell, 1958; Muehlberger, 1981; Garfunkel et al., 1981). In the

* Corresponding author. Tel.: +39 091 6809409; fax: +39 091 6809449.
E-mail address: walter.dalessandro@ingv.it (W. D'Alessandro).

http://dx.doi.org/10.1016/j.chemgeo.2014.09.006
0009-2541/

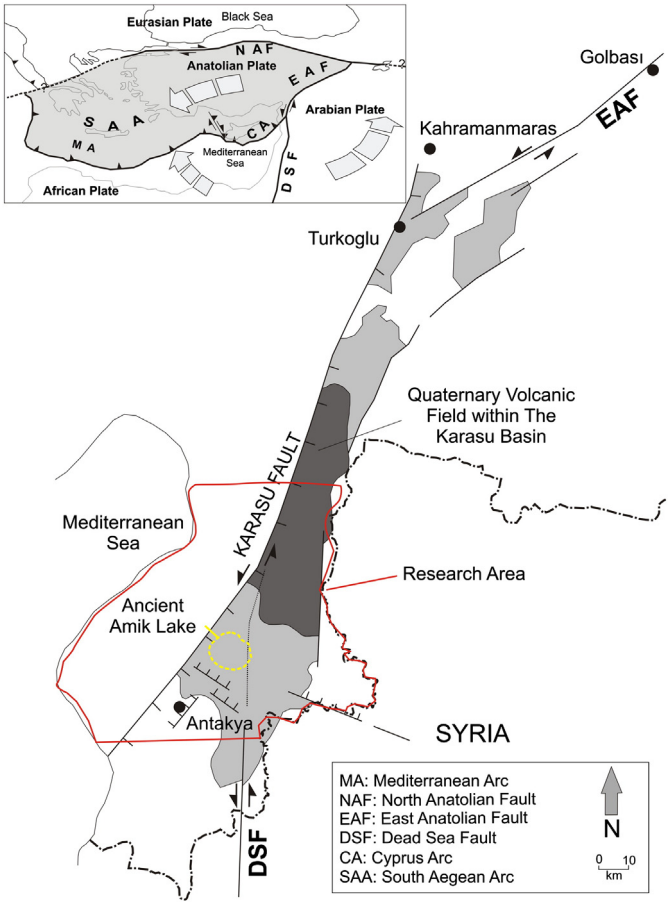

Fig. 1. Sketch map of the study area in the mainframe of the three tectonic plates.

Amik Plain, the DSF goes along the Asi (Orontes) River which has a sharp turn due to (Fig. 2, Karabacak et al., 2010) the connection of Amik Basin (Hatay Region, Turkey) with the SW extension of the Karasu Fault connecting the Dead Sea Fault (DSF) and East Anatolian Fault (EAF) (Fig. 1).

The seismic activity of the area is widely documented throughout history and several strong earthquakes were recorded (Boulton and Robertson, 2008). Among them the most destructive happened in 526 (that caused about 250,000 casualties) and in 1114, 1822 and 1872, all with estimated magnitudes ≥ 7.

Two rock units of particular interest for this study outcrop at the margins of the basin: an ophiolitic block located on the west (African Plate) and basalts located on the east and north-east (Arabian Plate).

This paper accounts for the geochemical features of the fluids (thermal and cold waters as well as seepage and bubbling gases) vented from the southern border of the Amik Basin to the northern sector of Karasu Fault Zone. The basin hosts several aquifers located at different depths. Both hypothermal and cold waters are vented by springs located on both sides of the DSF. Moreover, large amounts of groundwater are pumped from recently drilled boreholes for agricultural purposes.

Samples of fluids including both gases and waters from all the above-mentioned sources have been collected with the aim to define the origin, interactions, mixing as well as to trace the occurrence of other processes involving both gaseous and liquid fluids over the tectonically active area of the Amik basin.

2. Geological and tectonic background

Following the Late Cretaceous to Miocene progressive collision of the African–Arabian plate with the Eurasian (closure of northward subducting southern Tethys, the Bitlis–Zagros Ocean, Sengör and Yılmaz, 1981), the Anatolian block migrated towards west-southwest along the "Eastern Mediterranean Arc" onto the African oceanic plate

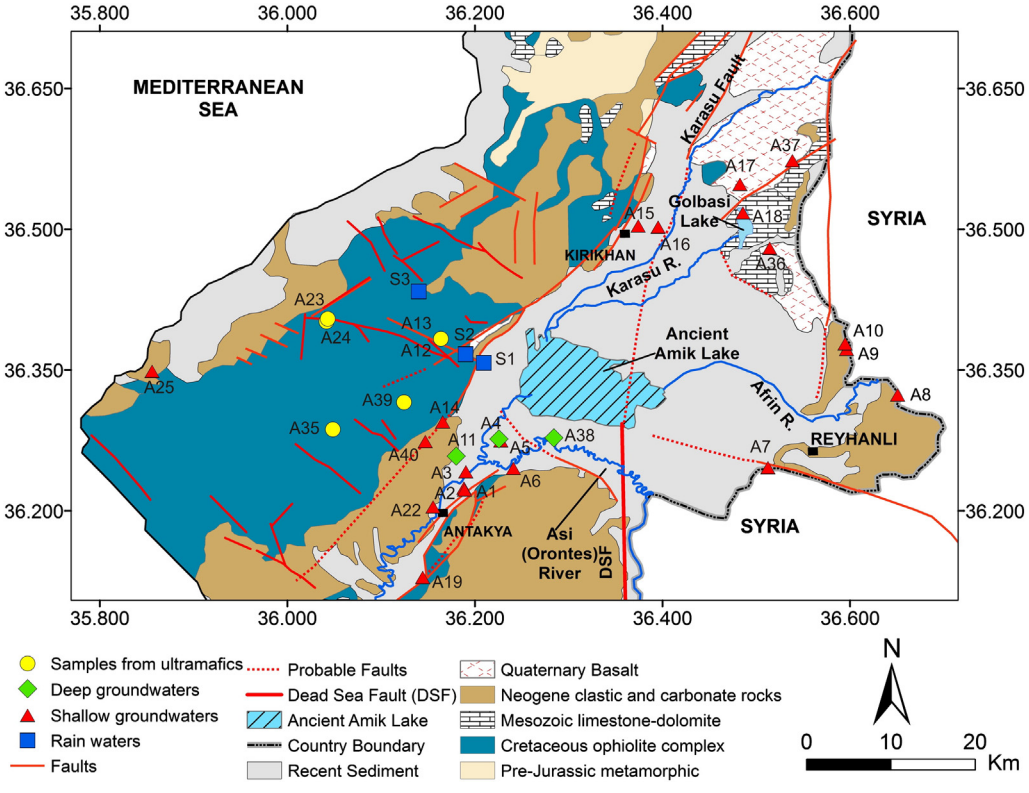

Fig. 2. Simplified geologic map with the sampling points. See Table 1 for sampling site details and coordinates.

(Fig. 1) (McKenzie, 1972; Sengor and Yılmaz, 1981; Hempton, 1987; Barka and Reilinger, 1997). This lateral extrusion of the Anatolian block is accommodated by two major continental transform faults: the North Anatolian Fault (NAF) and the East Anatolian Fault (EAF) zones. The EAF linked with the northward propagating Dead Sea Fault (DSF) during Latest Miocene in correspondence with the beginning of the oceanic spreading of the Red Sea during the last 4.5 Ma (Hempton, 1987). The Karasu Rift Basin started to evolve during this episode.

The Amik Basin — southern part of the Karasu Rift — is the intersection domain of several active, regional-scale structural lineaments namely the NS striking sinistral Dead Sea Fault (DSF), the NE striking sinistral East Anatolian Fault (EAF) and the NE striking contractional Cyprus Arc (CA) (Fig. 1).

The relationship between the EAF and the DSF is important as it displays a triple junction between the Arabian Plate, African Plate and Anatolian Block (e.g. Over et al., 2004; Mahmoud et al., 2013). The DSF is a sinistral transform fault that comprises various rift basins (Quennell, 1958; Freund et al., 1968; Garfunkel et al., 1981), more than 1000 km long, and links the Red Sea, where crustal spreading takes place, to the Tauride collision zone (Fig. 1). It is a seismically active tectonic structure crossing Israel, Jordan, Syria and Turkey following a nearly N–S direction where splays out after Ghab area (western Syria) (e.g. Quennell, 1958; Muehlberger, 1981; Garfunkel et al., 1981). The Karasu region is located within a seismically active region with significant activity since historical times (e.g. Akyüz et al., 2006). The most recent earthquakes clearly show that the region is still seismically active and originated from a NE–SW sinistral faulting with a normal dip-slip component in Karasu Region (Erdik et al., 1997).

The studies on slip rates, based on field observations, subsurface geophysical data and GPS data, suggest that the DSF Zone branches in southern Turkey (e.g. Muehlberger, 1981) and, thus the slip rate is partitioned and accommodated south to north (e.g. Chaimov and Barazangi, 1990). Due to above facts, there is a wide range of proposed slip rates for EAF, Karasu Fault and DSF.

Proposed slip rates for EAF zone are as follows: 4–10 mm/year by Kuran (1980); 9 mm/year by Kasapoglu (1987); 7.8–9 mm/year by Yürür and Chorowicz (1988); 29 mm/year by Taymaz et al. (1991); 19 mm/year by Lyberis et al. (1992); 6 mm/year by Kiratzi (1993); 6 mm/year by Westaway (1994).

Proposed local slip rates for the Karasu Fault segment are as follows: 4.01 mm/year by Rojay et al. (2001), 1.0 to 1.6 mm/year by Yurtmen et al. (2002), 2.89 mm/year by Seyrek et al. (2007), and 4.94 mm/year by Karabacak et al. (2010). The combined estimated sinistral slip rate across the DSF in the Karasu Rift is calculated to be as high as nearly 6 mm/year (Westaway, 2004) and 5.57 mm/year (Seyrek et al., 2007). Based on displaced archaeological relics in the Amik Basin, about 6.0 to 6.25 mm/year slip rate is suggested by Altunel et al. (2009) for the northern part of the DSF in Amik Basin.

Proposed slip rates for the DSF zone are 6 to 8 mm/year (Garfunkel, 1981); 11 mm/year (Kasapoglu, 1987); 3.8–10.0 mm/year (Quennell, 1958; McKenzie, 1972; Westaway, 2004), 7.0 mm/year (Gomez et al., 2007), and 3.0–7.5 mm/year (e.g. Meghraoui et al., 2003), and for Ghab segment of DSF is 4 to 5 mm/year by Westaway, 1994.

Additionally, geodetic technique has been used to estimate a slip rate along the DSF, however different values obtained from GPS studies. McClusky et al. (2003) and Reilinger et al. (1997, 2006) suggest that the slip rate changes between 4 and 8 mm/year along the DSF and the slip increases towards north. On the other hand, other estimated average slip rates for the DSF is 3.3 mm/year (e.g. Wdowinski et al., 2004) and up to 4.9 mm/year (e.g. Le Beon et al., 2008). The average slip rate for the DSF in Syria is 1.4 to 4 mm/year according to Gomez et al. (2007), about 6.9 mm/year according to Meghraoui et al. (2006) and 1.8 to 3.3 mm/year according to Alchalbi et al. (2010).

As seen from the literature, there is a wide range of proposed slip rates depending on the tools that differ from region to region, technique to technique and during each geological episode and it is difficult to propose a narrower range for the slip rate along the Arabian–African boundary.

The evolution of the Karasu Rift Valley (Antakya, SE Turkey) can be related to the DSF, or to the EAF, or to the combination of two or to the transition zone between them. The rift is interpreted as a pull-apart basin (Karabacak and Altunel, 2013.) or a half-graben resulted from flexural bend (Lyberis et al., 1992) or a graben resulting from divergent strike–slip motion (Muehlberger, 1981; Rojay et al., 2001) or a graben resulting from the westward escape of Anatolian plate (Yürür and Chorowicz, 1998). The rift is evolved in a contemporaneous transition from transpression to transtension in a left lateral shear zone with sinistral clockwise rotated block-bounding faults (Tatar et al., 2004). Fault slip data manifests a sinistral strike slip faulting in Karasu Rift (Yürür and Chorowicz, 1998; Rojay et al., 2001; Tatar et al., 2004; Altunel et al., 2009; Karabacak et al., 2010). On the other hand, the seismicity data point to crustal extension (Kiratzi, 1993) while GPS data favour a transtensional model (Barka and Reilinger, 1997; Reilinger et al., 1997, 2006; McCusky et al., 2000, 2003; Meghraoui et al., 2011).

The Karasu Basin developed between east dipping NNE striking faults of Karasu Fault which defines the western margin of the Rift where eastern block is downthrown and west dipping N–S to NNE striking faults of DSF system which controls the central part and eastern margin of the Rift where western block is downthrown (e.g. Rojay et al., 2001; Karabacak and Altunel, 2013).

The Karasu Basin is a well-recognized morphological depression bounded by highly elevated shoulders. The Amik depression, located at the southern part of the Karasu Rift at an altitude of about 80 m, corresponds to the widest and deepest part of the rift, and is the depocenter of the basin (Figs. 1, 2). The eastern and western margins of the rift display morphological differences. The western margin of the rift (the Amanos Mountains) is uplifted to a height of up to 2250 m. The eastern margin, on the other hand, has relatively low topography where its maximum height is 800 m. This geomorphological asymmetry reflects the asymmetric evolution of the basin. The major rivers (Karasu, Afrin and Asi) flow to the centre of the basin (Amik Lake), which are drained by the Asi (Orontes) River into the Mediterranean Sea at Samandag area (Figs. 1, 2). In the Amik Plain, the DSF goes along the Asi River which has a sharp turn and continue to flow towards W–SW (Fig. 1).

2.1. Distribution of rock units

The stratigraphic units of the area can be grouped into paleo- and neo-tectonic units that were emplaced during paleotectonic and neotectonic periods, respectively. The Late Cretaceous to Miocene paleotectonic period is related with the closure of the northward subducting southern Tethys (closure of the Bitlis-Zagros Ocean — Sengör and Yılmaz, 1981). The propagation of the DSF and linkage of the DSF with the EAF zone during Late Miocene mark the beginning of the neotectonic period in the area.

Paleotectonic units are the pre-Pliocene basement rocks that consist of Cretaceous ophiolite and ophiolitic complex overthrusted onto the pre-Cambrian to Campanian units and the Campanian–Maastrichtian to Miocene cover units. The Cretaceous ophiolite and ophiolitic complex, which are equivalents of the Baër-Bassit and the Troodos ophiolites, have an extensive spatial distribution in the region (Dilek and Thy, 2009) and are made up of ultramafic tectonites, mafic and ultramafic cumulates, gabbros, sheeted dyke complexes, plagiogranites, pillow lavas, bedded cherts and pelagic limestones. The ophiolite was emplaced over the autochthonous Cambrian to Campanian units of the African–Arabian Plate before the Maastrichtian and was lately overlain by Campanian–Maastrichtian to Miocene units (Tekeli et al., 1983). The Plio-Quaternary fluvial clastics and terraces deposited during the neotectonic phase are found only in the depressions like Amik, Karasu and Antakya, and are not observed on the rift shoulders (Boulton et al., 2006). Quaternary alkali basaltic volcanics (from 1.57 to 0.05 Ma) due to neotectonic activity are observed along margins,

centre and on the shoulders of Karasu Rift (Fig. 2) alternating with Plio-Quaternary basin fill clastics (Çapan et al., 1987; Rojay et al., 2001).

2.2. Hydrogeological outline of the area

The main surface runoff in the Amik Basin is provided by the Asi (*Orontes*) River and its tributaries, the Karasu and the Afrin Rivers, discharging in the Mediterranean Sea. The ancient Amik Lake, once in the middle of the Amik Basin, was drained to the Asi River by the State Hydraulic Works (DSI) of Turkey around half century ago.

Aquifers in the Amik Basin are composed of three groups from shallow to deep conditions: 1) Plio-Quaternary fluvials, Quaternary alluvium and alluvial fans capped by alternating Quaternary basalt; 2) Miocene aged limestone and conglomerates; and 3) Cretaceous to Eocene aged mostly karstified limestones. The last one is a confined aquifer while the first two are representative of semi-confined or unconfined conditions. The youngest aquifer composed of basalts crops out in the northern and eastern sectors of the basin. The alluvial fans and alluvium are very productive aquifers with thickness reaching up to 200 m in the middle of the basin. Limestone aquifers generally emerge at the margin of the basin in the east and south as well as in the north. In general surface and groundwater flow direction in the Basin is towards the ancient Amik Lake which is currently drained to the Mediterranean Sea along the Asi River.

Karstified limestones at the south (Harbiye town) and southeast (around Reyhanli town) together with the Golbasi karstic discharge in the east of basin near Kirikhan town are the most important fresh water aquifers in the area. Tectonic factors control groundwater circulation system in the Reyhanli district composed of complex horst-graben compartments (Yuce, 1999, 2007). The aforementioned karstic discharges with the large karst springs are utilized by the local municipalities for potable and irrigation demands.

The groundwater potential of Amik Basin was estimated in 130 hm^3/a by DSI in 1979. However, actual groundwater consumption, taking into consideration withdrawing from the wells, was assumed to be three times the recharge. Over-extraction of groundwater caused a dramatic depression of the groundwater table and a considerable decrease of the spring yields.

3. Sampling and analytical methods

A suite of samples composed of both waters and gases to be analysed for their chemical and isotopic composition were collected during two field campaigns in August 2012 and June 2013. The full samples list taken at 27 different sites is shown in Table 1, including the sample locations as well as the altitude, the source type and the depth of the wells.

Six rainwater samples were collected at three sites located at different altitudes to get an insight into the local meteoric recharge. Samples represent the integrated bulk deposition of several months covering the period from October 2012 to March 2013. Rain gauges were built up to minimize evaporation by liquid paraffin added to form a 5 mm thick layer over the collected rainwater. Further information about the rainwater sampling device can be found in Bellomo et al. (2003) and D'Alessandro et al. (2004).

Water temperature, pH, Eh and electric conductivity were measured in the field by portable instruments. All chemical and isotopic analyses on water samples except for tritium were carried out at the INGV-Palermo geochemical laboratories. Total alkalinity was determined by titration with 0.1 M HCl on unfiltered samples. Major anions (F^-, Cl^-, NO_3^- and SO_4^{2-}) were determined by ionic chromatography on filtered samples. Major cations (Na^+, K^+, Mg^{2+} and Ca^{2+}) by ionic chromatography on filtered and acidified (0.2% HNO_3) samples.

Spectrophotometric methods were used for the determination of NH_4 (Berthelot's reaction).

Table 1
List, description and location of the sampling sites. The numbers in "Type" column indicate that the sampling site is a well and represent the well depth (m), S = spring, GS = gas seepage, RG = rain gauge.

Site ID	Site name	Type	Latitude	Longitude	Altitude
A1	Ozbugday flour factory	60	36.2243°	36.1883°	103
A2	Soguksu karstic spring	S	36.2223°	36.1889°	103
A3	Guzelburc	60	36.2416°	36.1903°	91
A4	Ottoman Palace	1270	36.2766°	36.2255°	78
A5	Ottoman Palace	130	36.2746°	36.2276°	73
A6	Ili Pinar	S	36.2453°	36.2411°	108
A7	Cayir	100	36.2460°	36.5124°	97
A8	Borniaz	450	36.3235°	36.6508°	75
A9	Hamamat	S	36.3720°	36.5963°	127
A10	Hamamat cold spring	S	36.3780°	36.5947°	119
A11	Honda Deep well	1200	36.2584°	36.1800°	91
A12	Tahtakopru	S	36.3835°	36.1636°	275
A13	Tahtakopru	S	36.3835°	36.1636°	275
A14	Karaali thermal well	80	36.2948°	36.1656°	166
A15	Kirikhan well	56	36.5034°	36.3741°	119
A16	Kirikhan irrigation well	96	36.5022°	36.3953°	111
A17	Golbasi lake	44	36.5479°	36.4825°	95
A18	Golbasi lake karstic spring	S	36.5173°	36.4857°	60
A19	Harbie karstic spring	S	36.1291°	36.1442°	247
A22	Antakya Ogretmenevi	110	36.2042°	36.1553°	100
A23	Kurtbagi	GS	36.4018°	36.0416°	540
A24	Kurtbagi	GS	36.4047°	36.0429°	471
A25	Kokarca Spring/Tulek	S	36.3486°	35.8558°	23
A35	Kisecik	S	36.2869°	36.0484°	731
A36	Sucu village well	100–150	36.4798°	36.5142°	147
A37	Yalangoz–Incirli	100–150	36.5730°	36.5384°	159
A38	Yesilova MTA well	750	36.2779°	36.2842°	87
A39	Gulderen	S	36.3159°	36.1242°	661
A40	Kuzey Tepe	450	36.2738°	36.1471°	204
S1	Serinyol	RG	36.3576°	36.2093°	120
S2	Tahtakopru	RG	36.3670°	36.1900°	190
S3	Komurcukuru	RG	36.4337°	36.1400°	880

Water isotopic composition in terms of $\delta^{18}O$ and δD was determined by mass-spectrometry on unfiltered samples and expressed in ‰ with respect to the international standard V-SMOW (Vienna Standard Mean Ocean Water). The uncertainties are ±0.1‰ for $\delta^{18}O$ and ±1‰ for δD (±1σ).

The tritium content was measured at the Hacettepe University laboratory using electrolytic enrichment and liquid scintillation spectrometry. The results are expressed in tritium units (TU) (one TU is equivalent to one ^3H atom per 10^{18} atoms of hydrogen) with the analytical uncertainty in the order of 0.3 TU.

Twenty-seven samples for dissolved gas analyses were collected in glass vials sealed underwater. Three free bubbling gas samples were taken by an inverted funnel and 3 free gases were collected at dry seeps by inserting a pipe in the soil and driving the soil gas to the sampling bottle by a syringe and a 3-way valve. All free gas samples were stored in Pyrex bottles with two vacuum stopcocks.

The collected samples have been delivered to the laboratory by express courier in order to bring to the end the analytical job within two-three weeks after the sampling (Italiano et al., 2014).

In the laboratory, the chemical analyses were carried out by gas chromatography (Perkin Elmer Clarus 500 equipped with a double Carboxen 1000 columns, TCD-FID detectors) using argon as the carrier gas. Typical uncertainties were within ±5%. The free gases were directly injected in the gas chromatograph, while dissolved gases were extracted after equilibrium was reached at constant temperature with a host-gas (high-purity argon) injected in the sample bottle. Details on the analytical procedure are reported in Italiano et al. (2009a, 2014) and Liotta and Martelli (2012).

C_1–C_5 hydrocarbons were analysed in a few free gas samples using a Shimadzu 14a GC equipped with FID and a packed Chromosorb PAW 80/100 column. The measurement precision was better than ±5% for common gases and ±10% for trace gases such as the alkenes.

The He-isotope ratio in free gas samples was analysed directly from the sample bottles after purification in the high-vacuum inlet line of the mass spectrometer. The isotope composition of dissolved He was analysed by headspace equilibration, following the method proposed by Inguaggiato and Rizzo (2004) and Italiano et al. (2014). He and Ne were then cryogenically separated and admitted into mass spectrometers. The $^3He/^4He$ ratio and ^{20}Ne content were analysed by a GVI Helix SFT mass spectrometer. Helium isotope compositions are given as R/R_A, namely $^3He/^4He$ of the sample versus the atmospheric $^3He/^4He$ ($R_A = 1.386 \times 10^{-6}$). Measured values were corrected for the atmospheric contamination of the sample (R_C/R_A) on the basis of its $^4He/^{20}Ne$ ratio (Sano and Wakita, 1985).

Isotopic composition of CO_2–C was analysed with a mass spectrometer (Finnigan MAT Delta S) after purifying the CO_2 under vacuum. $\delta^{13}C$ values of total dissolved inorganic carbon (TDIC) were determined by acid extraction following the method proposed by Capasso et al. (2005). Isotopic compositions of CH_4–C, CH_4–H and H_2–H were measured using a Thermo TRACE GC and a Thermo GC/C III interfaced to a Delta Plus XP gas source mass spectrometer. $^{13}C/^{12}C$ ratios are reported here as $\delta^{13}C$ values (±0.1‰ for CO_2 and ±0.2‰ for CH_4) with respect to the V-PDB standard. H/D ratios are reported here as δD values (±2‰ for CH_4 and ±5‰ for H_2) with respect to the V-SMOW standard.

4. Results

4.1. Water geochemistry

Results of the chemical and isotopic analyses of the sampled groundwater and rainwater are listed in Table 2. Measured temperatures are generally below 30 °C and only 5 samples exceed 35 °C with maximum temperature of 42.8 °C. Groundwater samples display wide ranges for pH (6.61–12.15), electrical conductivity (450–44,150 μS/cm) and Eh (−870 to 476 mV). They can be roughly identified as 3 groups: 1) deep, 2) hyperalkaline and 3) shallow groundwaters. The first group includes 5 water samples (A4, A11, A4-2, A11-2, A38) collected from deep drillings (>1000 m) that are characterised by high salinities (TDS 7900–33,000 mg/l) and sodium-chloride composition (Fig. 3). The second group is composed of 4 samples (A12, A12-2, A35, and A39) collected from springs issuing within the ophiolitic complex. These are hyperalkaline waters (pH 10.59–12.15) with Ca–OH composition and very low sulfate and Mg concentrations typical of waters deeply circulating in ophiolitic rocks (Cipolli et al., 2004). The remaining samples have been grouped together despite a large variety in composition ranging from Ca–HCO_3 and Ca–Mg–HCO_3 to Mg–HCO_3 and Na–Ca–Cl–SO_4. The name "shallow groundwater" is purely indicative as some of them having a deep circuit. They were mostly collected from shallow wells (<150 m) within the Amik Basin or from springs at the feet or on the flank of the surrounding hills and mountains. Only two wells (A8 and A40) have depths around 450 m. The waters with bicarbonate as the main anion have low salinity (TDS 394–985 mg/l) while those with chloride or/and sulfate as the major anion display a slightly higher salinity (TDS 866–1840 mg/l) and were collected from thermal springs or wells (30.3–38.0 °C). These are referred as thermalized shallow groundwaters.

Rainwater samples have expectedly very low salinity (TDS 15–31 mg/l) and display a Ca–HCO_3 composition (Fig. 3) which is typical for the Mediterranean rainfall (Al-Momani et al., 1995; Yuce, 2005; D'Alessandro et al., 2013 and references therein). Their isotopic composition plotted in Fig. 4, ranges from −8.20 to −4.47‰ and from −46.0 to −16.7‰ for $\delta^{18}O$ and δD, respectively. Regarding oxygen–hydrogen isotope compositions, hyperalkaline groundwaters display the most negative values ($\delta^{18}O$ from −8.74 to −7.87‰; δD from −45.0 to −40.2‰), in contrast to waters from the deep wells having the most positive values ($\delta^{18}O$ from −4.53 to −1.22‰; δD from −25.9 to −7.9‰). The shallow groundwaters show intermediate values ($\delta^{18}O$ from −7.27 to −4.63‰; δD from −39.4 to −23.6‰).

Tritium values range from 0 to 5.38 TU with the highest values falling in the range of the regional meteoric recharge (Yuce, 2001; Al-Charideh and Abou Zakhem, 2010; Al-Charideh, 2011). Deep, hyperalkaline and thermalized shallow groundwaters show generally low to undetectable tritium values pointing to a longer hydrologic circulation in the aquifer systems.

The measured $\delta^{13}C_{TDIC}$ values range from −15.99 to −4.98‰. The samples referring to groundwaters characterised by longer circuits (lower tritium values) show generally $\delta^{13}C_{TDIC}$ values higher than −10‰.

4.2. Gas geochemistry

The chemical composition of the dissolved gas phase was obtained from the gas chromatographic analyses taking into account the solubility coefficients (Bunsen coefficient "β", cc_{gas}/ml_{water} STP) of each gas species, the volume of gas extracted and the volume of the water sample (details in Liotta and Martelli, 2012 and Italiano et al., 2009a, 2014). Starting from the total amount of dissolved gases (ccSTP/l) we calculated the relative abundances for every single gas species in equilibrium with the dissolved gas phase and expressed the analytical results in μmol/mol, allowing the comparison of both dissolved and free gas results (Table 3).

Only three sites with venting gases have been identified until now in the study area. Two sites show bubbling gases, one in the hyperalkaline spring of Tahtakopru (A12) and the other in the karstic spring on the Golbasi Lake shore (A18). The third site, called Kurtbagi, located within the ophiolitic massif, presents dry soil gas seepage that sometimes ignites, closely resembling the everlasting fires of the more famous manifestations of Chimaera (Çıralı, Antalya Gulf, Turkey — Etiope et al., 2011). In Kurtbagi two seeps, about 200 m apart from each other, were sampled.

Results of the chemical and isotopic analyses of dissolved and free gases are shown in Tables 3 and 4.

The composition of the gas phase dissolved in shallow groundwaters is dominated by atmospheric gases ($O_2 + N_2$) which together account for at least 884,000 μmol/mol. After the atmospheric gases, the most abundant gas in the shallow groundwater samples is CO_2 that ranges from 105 to 111,800 μmol/mol. Methane ranges from <1 to 5120 μmol/mol with the highest values corresponding to samples with high N_2/O_2 ratios. Hydrogen is generally below detection limit and only 7 shallow groundwater samples show values from 5 to 80 μmol/mol.

The groundwaters collected from the deep wells have all CH_4 as the prevailing gas species (625,500–863,200 μmol/mol), high N_2 contents (135,000–369,700 μmol/mol) connected with high N_2/O_2 ratios (124–214), low CO_2 (915–3090 μmol/mol) and very low H_2 (<25 μmol/mol) contents.

The samples collected from the hyperalkaline springs and from the dry gas seeps have variable composition but they have in common a very low CO_2 concentration (<1200 μmol/mol). Almost all samples have high H_2 concentrations (35,000–605,000 μmol/mol), this gas being the prevailing species in the Tahtakopru bubbling gas. The exception is sample A35, where H_2 is below detection limit. Methane is also an important, sometimes prevalent, gas species (119,300–607,400 μmol/mol). The dry gas seeps have low N_2 concentrations (<25,000 μmol/mol) and N_2/O_2 ratios (4.2–13) close to the atmospheric one of 3.7, while the gases collected from the hyperalkaline springs have higher N_2 contents (279,100–797,300 μmol/mol) but also generally high N_2/O_2 ratios (up to 2800).

Light gas alkanes (C_2–C_5) have been measured only in the dry gas seeps and in the free gas bubbling in the hyperalkaline spring of Tahtakopru (Table 4). The former shows a total concentration of light alkanes of about 9000 μmol/mol and a $C_1/(C_2 + C_3)$ ratio of about 90 while the latter has much lower total concentration (~100 μmol/mol) and higher ratio (>2400).

Table 2
Chemical and isotopic composition of the water samples collected in the Amik Basin area. TA = total alkalinity expressed as HCO_3^-; TDS = total dissolved solids; $\delta^{13}C$ = C-isotopic composition of total dissolved inorganic carbon (TDIC); nm = not measured; nd = not determined.

Sample	Date	pH	T	Cond	Eh	Na^+	K^+	Mg^{2+}	Ca^{2+}	F^-	Cl^-mg/l	NO_3^-	SO_4^{2-}	TA	SiO_2	NH_4^+	TDS	$\delta^{18}O$	δD	^3H	$\delta^{13}C$
	dd-mm-yyyy		°C	µS/cm	mV	mg/l	mg/l	mg/l	mg/l	mg/l	mg/l	mg/l	mg/l	mg/l	mg/l	mg/l	mg/l	‰	‰	TU	‰
Shallow groundwater																					
A1	04-08-2012	7.15	20.0	560	nm	13.3	2.62	31.0	67.7	0.13	23.3	1.1	40.1	311	26.7	nd	517	−6.39	−31.1	4.73	−14.28
A2	04-08-2012	7.49	21.0	502	nm	11.9	0.86	27.4	59.3	0.16	24.1	11.7	32.0	268	20.2	nd	456	−6.46	−31.3	5.38	−12.94
A3	04-08-2012	7.19	21.0	1076	nm	42.6	0.95	106	55.0	0.07	60.8	17.4	89.9	580	32.3	nd	985	−6.10	−29.8	3.52	−15.99
A5	04-08-2012	7.55	22.1	648	nm	15.5	0.69	29.5	58.5	0.13	23.5	21.5	15.8	293	43.1	nd	501	−5.63	−26.3	4.13	−14.70
A6	04-08-2012	7.40	22.6	587	nm	16.0	1.27	37.1	60.7	0.23	25.2	11.1	37.2	329	28.8	<0.002	547	−6.39	−31.7	3.79	−13.57
A7	04-08-2012	7.10	23.3	959	nm	33.6	4.27	38.8	129	0.42	50.0	35.2	176	348	20.6	<0.002	836	−6.00	−32.5	1.23	−12.41
A8	04-08-2012	7.30	29.0	747	nm	24.8	4.74	30.2	94.3	0.48	39.3	16.7	78.5	305	20.7	nd	615	−6.71	−36.6	0.00	−8.66
A9	07-08-2012	6.61	37.7	2461	15	315	29.6	40.6	166	2.42	411	<1	376	458	40.0	nd	1840	−6.97	−39.5	0.13	−5.63
A10	07-08-2012	6.93	25.8	619	nm	27.2	1.32	18.4	87.2	0.46	36.5	11.7	27.8	317	27.2	nd	555	−6.79	−36.7	0.73	−11.32
A14	07-08-2012	9.02	30.3	1112	128	257	1.02	0.15	28.1	0.21	178	0.29	335	36.6	29.2	0.084	866	−7.11	−37.1	0.15	nd
A15	08-08-2012	7.07	28.9	990	252	28.5	3.61	66.0	87.1	0.66	47.1	61.5	101	390	45.4	nd	831	−6.81	−35.5	4.28	−13.74
A16	08-08-2012	6.92	31.2	1347	239	80.1	9.76	67.8	133	1.84	59.2	39.0	469	253	69.1	<0.002	1183	−6.56	−34.8	3.81	−9.43
A17	08-08-2012	7.30	22.0	662	263	21.6	0.21	45.0	58.4	0.24	18.6	7.09	104	296	46.3	nd	597	−6.83	−36.1	1.41	nd
A18	08-08-2012	6.92	23.1	639	283	10.2	1.94	32.4	72.6	0.31	12.4	15.9	88.3	268	23.5	nd	526	−7.27	−39.4	3.68	−8.74
A19	08-08-2012	7.14	16.3	450	476	5.73	0.60	16.7	67.4	0.15	9.91	7.94	6.66	262	16.2	0.004	394	−7.15	−36.1	4.57	−12.93
A22	09-08-2012	7.10	19.7	760	291	28.3	0.61	47.3	77.2	0.12	43.4	24.4	33.6	400	54.8	<0.002	709	−6.44	−31.2	4.23	−14.83
A25	14-08-2012	7.40	22.5	1152	105	105	2.22	86.6	29.1	0.79	73.5	1.87	184	403	9.5	nd	896	−4.63	−23.6	2.75	−14.56
A1-2	24-06-2013	nm	20.2	573	nm	13.8	2.23	33.1	73.9	0.14	23.1	17.0	40.3	323	25.6	nd	553	−5.85	−27.8	nd	nd
A2-2	24-06-2013	nm	20.4	499	nm	12.0	0.91	30.5	61.4	0.14	21.5	13.2	31.7	262	20.0	nd	454	−5.89	−28.8	nd	nd
A3-2	24-06-2013	nm	19.6	992	nm	41.5	0.66	105	57.8	0.04	53.2	18.9	77.3	555	31.6	nd	941	−5.89	−29.3	nd	nd
A9-2	28-06-2013	6.66	38.0	2367	−282	315	28.9	48.0	131	2.11	354	<1	353	445	39.0	nd	1718	−6.70	−38.9	0.42	−5.40
A18-2	28-06-2013	7.20	22.5	613	174	11.3	1.84	34.4	87.8	0.27	11.9	18.2	86.7	323	24.7	<0.002	600	−6.82	−37.0	3.76	nd
A36	28-06-2013	6.93	21.8	705	40	21.2	1.43	31.9	94.6	0.31	40.4	32.6	38.8	348	32.0	<0.002	641	−6.28	−33.2	2.64	−13.49
A37	28-06-2013	7.26	22.1	573	67	9.7	1.32	31.2	80.6	0.25	9.01	11.9	64.3	323	21.0	<0.002	553	−7.20	−38.0	4.55	−12.45
A40	25-07-2013	7.50	37.6	1806	nm	276	5.38	10.3	41.1	0.58	231	2.7	361	91.5	29.2	nd	1050	−7.17	−36.2	0.15	nd
Deep groundwater																					
A4	04-08-2012	7.30	42.8	43,300	nm	10,100	68.2	224	1030	<1	17,600	<10	18.6	67.1	18.4	51.8	29,208	−1.82	−8.5	0.11	nd
A11	07-08-2012	7.96	32.6	12,470	−151	2960	19.2	25.2	81.7	<0.5	4640	<5	8.02	146	21.3	13.7	7922	−4.53	−25.1	0.07	nd
A4-2	26-06-2013	7.26	42.3	44,150	−202	10,100	50.2	278	1220	<1	18,800	<10	0.23	73.2	20.3	54.6	30,682	−1.22	−7.9	nd	nd
A11-2	24-06-2013	nm	28.8	13,062	nm	2980	13.0	30.6	102	0.70	4780	<5	0.48	177	21.9	nd	8141	−4.31	−25.9	0.45	nd
A38	29-06-2013	7.91	26.8	37,500	−28	11,000	57.5	360	1020	<1	19,900	<10	0.48	97.6	15.2	nd	32,662	−0.98	−8.0	0.75	nd
Hyperalkaline groundwater																					
A12	07-08-2012	10.59	33.7	819	−870	49.9	1.77	0.13	44.7	0.005	47.6	<0.1	0.20	183	0.2	0.062	327	−8.74	−45.0	1.64	nd
A35	26-06-2013	11.58	25.5	1090	−185	28.6	0.93	0.79	83.4	0.005	45.8	<1	0.005	244	0.24	<0.002	404	−7.87	−40.2	0.00	nd
A12-2	28-06-2013	11.61	33.0	786	−507	50.3	2.07	0.42	42.1	0.008	44.5	<1	0.02	177	0.17	0.16	317	−8.11	−42.1	nd	nd
A39	30-06-2013	12.15	21.7	1469	−590	55.0	1.22	0.10	110	0.005	72.1	<0.1	0.23	336	0.23	<0.002	575	−7.90	−41.3	0.31	nd
Rainwater																					
S1	18-01-2013	6.29	nm	nm	nm	0.81	0.23	0.15	3.61	0.008	1.61	1.73	4.36	13	nd	2.5	25	−7.40	−40.0	nd	nd
S2	18-01-2013	6.52	nm	nm	nm	0.74	0.35	0.18	2.09	<0.005	1.42	1.63	2.53	11	nd	2.54	20	−7.70	−42.0	nd	nd
S3	18-01-2013	6.74	nm	nm	nm	0.71	0.31	0.21	2.32	<0.005	1.44	1.15	3.81	5	nd	1.02	15	−8.20	−46.0	nd	nd
S1	20-03-2013	nm	nm	nm	nm	2.25	0.30	0.47	5.07	0.030	4.46	<0.1	5.90	9	nd	<0.04	27	−4.47	−16.7	nd	nd
S2	20-03-2013	nm	nm	nm	nm	2.22	0.39	0.40	3.92	0.029	4.24	0.17	4.13	15	nd	2.3	31	−4.53	−18.7	nd	nd
S3	20-03-2013	nm	nm	nm	nm	2.40	0.30	0.37	3.26	0.019	4.28	<0.1	4.76	7	nd	0.66	23	−6.14	−28.3	nd	nd

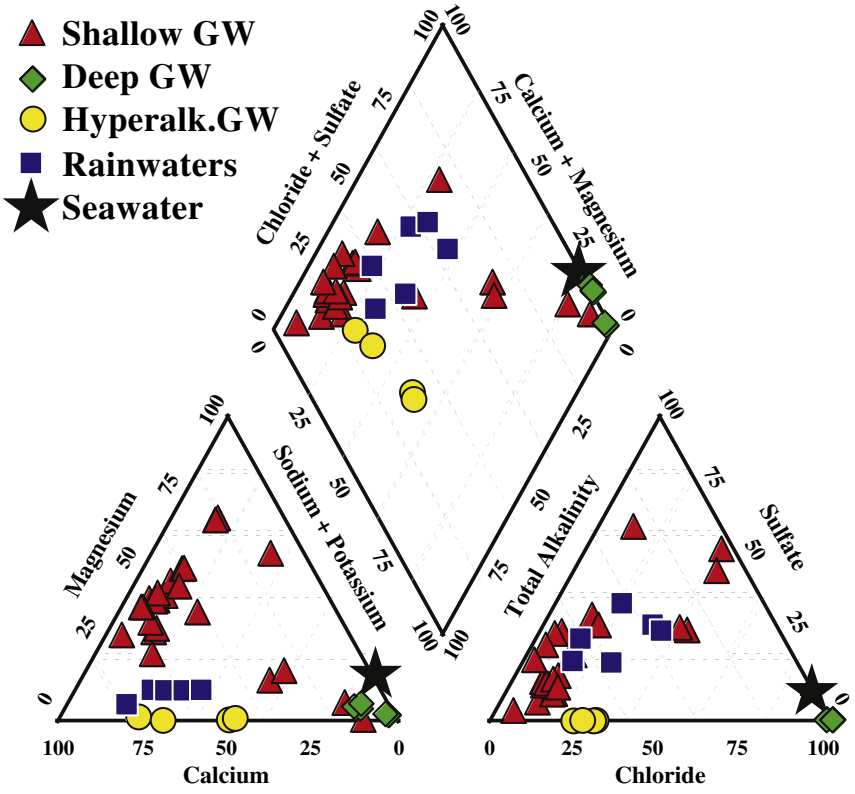

Fig. 3. Piper diagram showing the composition of the major ions in the sampled waters. The composition of seawater is evidenced with the star symbol.

The measured He isotope compositions range from 0.29 to 1.39 R/R_A (R_A = isotopic $^3He/^4He$ ratio in air = 1.39×10^{-6}). Due to the low $^4He/^{20}Ne$ ratios (<0.5) compared to the atmospheric ratio of 0.318, only a few helium isotopes values, ranging from 0.07 to 1.74 (R_C/R_A), were corrected for air contamination (Table 3) assuming that all neon was of atmospheric origin.

Most of the shallow groundwater samples display He contents and $^4He/^{20}Ne$ ratios close to air-saturated water (ASW @ 20 °C – He = 4.243×10^{-5} ccSTP/kgH_2O; $^4He/^{20}Ne$ = 0.2672; Holocher et al., 2002) consistent with their relatively high contribution of atmospheric components (Table 3). Only a few samples are enriched in He and among them some of the slightly thermalized groundwaters show enrichments up to two orders of magnitude. All the deep groundwaters show enrichments of nearly one order of magnitude of the dissolved He content compared to the atmosphere. A similar enrichment is found also in one of the dissolved gases collected in the hyperalkaline groundwaters (A12) while the remaining two have very low He concentrations, close to the equilibrium with the atmosphere.

Stable C- and H-isotopic composition of CH_4 in the dry gas seeps range from −5.5 to −4.8‰ and from −107 to −96‰ respectively, while free gas bubbling in the hyperalkaline spring of Tahtakopru shows values of about −30‰ for $\delta^{13}C$ and about −320‰ for δD. All these free gas samples display very negative δD (H_2) values ranging from −704 to −762‰.

Stable C-isotope composition of CH_4 in dissolved gases has been measured only on three samples. The hyperalkaline spring of A39 shows a $\delta^{13}C(CH_4)$ of −12.8‰ while the deep groundwater samples A4 and A11 show very similar values of about −65‰ (Table 4).

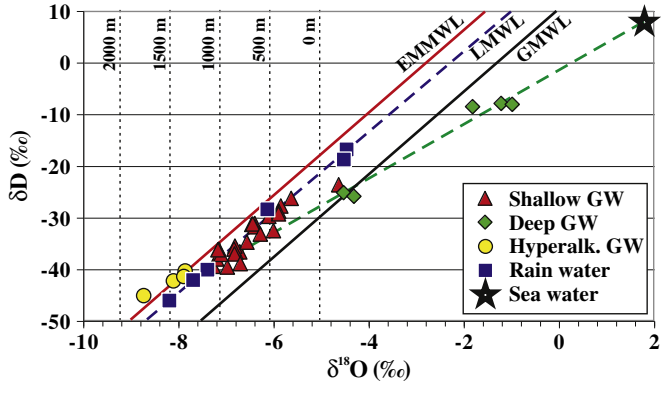

Fig. 4. δD–$\delta^{18}O$ binary plot. The Global Meteoric Water Line (GMWL, black line — Craig, 1961), the Eastern Mediterranean Meteoric Water Line (EMMWL, red line — Gat and Carmi, 1970), the Local Meteoric Water Line (LMWL, blue dashed line — Al-Charideh, 2011) and the Mediterranean Sea Water point are also shown. Mixing between seawater and local meteoric water is evidenced with a green dashed line. Vertical stippled lines indicate the mean recharge elevation obtained from the isotopic lapse rate ($\delta^{18}O = -0.0021 \times Alt - 5.03$, where Alt is altitude in m) of the area (Al-Charideh and Abou Zakhem, 2010). (For interpretation of the references to colour in this figure legend, the reader is referred to the web version of this article.)

5. Discussion

5.1. Isotope hydrology

The isotopic composition of the sampled water samples gives us precious information about the hydrologic circulation in the study area. Although we collected only a few rainwater samples and they are not enough to define a local meteoric water line, the regression line on which they fall ($\delta D = 7.68 \times \delta^{18}O + 17.3$) is almost indistinguishable from that described for close by areas of western Syria (Al-Charideh, 2011) indicating that meteoric recharge along the coastal area of eastern Mediterranean is very similar. Thereafter, we used the isotopic lapse rate ($\delta^{18}O = -0.0021 \times Alt - 5.03$, where Alt is altitude in m) defined for the same area (Al-Charideh and Abou Zakhem, 2010) to estimate the mean recharge altitude of the sampled

Table 3
Chemical and isotopic composition of free and dissolved gases of Amik Basin area. Sites in bold indicate free gas samples while the remaining indicate dissolved gas samples. nd = not determined; nc = not calculated; na = not applied.

Site	Date	He	H_2	O_2	N_2	CH_4	CO_2	P_{tot}	R/R_A	Error	$^4He/^{20}Ne$	R_C/R_A	A	C	M
	dd-mm-yyyy	μmol/mol						atm					%	%	%
A1	04-08-2012	9.3	<10	1220	982,200	6.2	16,550	0.7	nd	na	nd	nc	nc	nc	nc
A2	04-08-2012	6.0	46.0	147,700	847,000	2.4	5240	1.1	0.97	0.026	0.279	nc	96	4	0
A3	04-08-2012	5.5	<10	3570	991,300	3.7	5130	1.5	0.99	0.009	0.305	nc	87	11	2
A5	04-08-2012	11.4	<10	137,200	847,800	345	14,660	0.8	1.01	0.015	0.314	nc	85	13	2
A6	04-08-2012	5.1	<10	156,900	829,100	3.5	13,940	0.8	0.54	0.056	0.311	nc	82	18	0
A7	04-08-2012	9.9	<10	126,000	842,600	84	31,230	0.9	0.93	0.006	0.321	nc	83	15	2
A8	04-08-2012	6.1	<10	132,800	848,900	6.4	18,330	1.1	nd	na	nd	nc	nc	nc	nc
A9	07-08-2012	1660	<10	605	883,700	2240	111,800	1.0	1.04	0.011	13.5	1.05	2	82	16
A9-2	28-06-2013	1530	<10	3680	928,000	2035	64,730	1.2	1.12	0.016	11.7	1.12	2	81	17
A10	07-08-2012	10.5	41.0	33,410	930,500	19	35,990	0.7	0.89	0.002	0.315	nc	84	15	1
A14	07-08-2012	7.9	<10	13,320	986,600	1.1	105	1.1	0.70	0.011	0.352	nc	75	25	0
A15	08-08-2012	40.2	<10	122,000	860,500	4.6	17,470	1.1	1.01	0.007	2.11	1.01	13	74	13
A16	08-08-2012	333	79.9	76,430	911,300	183	11,720	1.4	0.98	0.007	11.9	0.98	2	83	15
A18	08-08-2012	18.7	17.5	138,700	843,400	227	17,640	0.6	1.16	0.010	1.13	1.22	24	62	14
A18-2	28-06-2013	44.0	5.0	125,300	837,600	0.7	15,100	na	1.14	0.009	0.520	1.36	61	31	8
A19	08-08-2012	11.2	34.7	168,000	820,900	181	10,900	0.7	0.90	0.056	0.272	nc	97	3	0
A22	09-08-2012	12.6	<10	45,940	929,200	259	24,580	0.8	0.98	0.010	0.316	nc	84	14	2
A25	14-08-2012	33.7	<10	642	978,700	2670	17,950	0.7	0.50	0.003	0.855	0.25	31	66	3
A36	28-06-2013	30.5	11.1	114,000	863,300	54	22,650	1.1	1.23	0.029	0.593	1.45	45	43	12
A37	28-06-2013	15.2	<10	152,900	834,300	<1	12,750	0.8	1.34	0.031	0.551	1.70	47	38	13
A40	25-07-2013	8.1	<10	3220	959,500	5120	32,200	1.3	0.62	0.002	0.482	0.08	55	44	1
A4	04-08-2012	23.6	25.2	1030	212,000	785,200	1760	0.8	0.35	0.002	1.29	0.16	21	77	2
A11	07-08-2012	34.7	13.6	850	135,000	863,200	915	1.2	0.31	0.001	1.08	0.07	25	74	1
A11-2	24-06-2013	39.5	<10	2480	307,900	688,400	1160	1.1	0.29	0.004	1.80	0.15	15	83	2
A38	29-06-2013	25.6	<10	1730	369,700	625,500	3090	1.3	0.41	0.003	0.863	0.13	31	68	1
A23	05-08-2012	29.0	371,200	1900	25,000	603,800	774	na	1.33	0.006	526	1.33	0	80	20
A24	05-08-2012	29.0	384,200	1800	12,600	607,400	983	na	1.24	0.006	516	1.24	0	81	19
A24-2	27-06-2013	26.0	379,800	5000	21,000	602,900	42	na	1.39	0.007	8.46	1.40	4	75	21
A13	07-08-2012	1.7	487,400	28,500	399,500	102,500	1200	na	0.98	na	0.311	nc	nc	nc	nc
A12	07-08-2012	30.1	499,900	410	380,300	119,300	27	0.9	0.98	0.028	3.94	0.98	7	79	14
A12-2	28-06-2013	4.5	605,000	100	279,100	120,300	41	na	1.96	0.038	0.404	nc	nc	nc	nc
A35	26-06-2013	7.9	<10	3650	797,300	197,900	1128	0.8	0.99	0.035	0.444	nc	60	34	6
A39	30-06-2013	40.8	35,000	55,200	621,200	288,600	<20	0.8	0.98	0.030	0.321	nc	83	15	2

groundwaters (Fig. 4). Excluding samples that are contaminated by a marine water component (deep groundwater), the range of the mean recharge altitudes for the shallow groundwaters is from 267 to 1065 m. The groundwaters with the mean recharge altitude higher than about 800 m testify how a consistent portion of the recharge comes from the coastal mountains to the west of the Amik Basin. The Amanous Mountain Range, whose highest peaks exceed 2000 m, represents an important condensation barrier for the humidity from the Mediterranean Sea. The 40-year mean precipitation value at Antakya is 1092 mm (TGDM, 2014) and increases with altitude up to values exceeding 1500 mm.

An alternative explanation of the most negative isotopic values could be the contribution of deep confined aquifers recharged during the Late Pleistocene cold periods. The presence of such aquifers has been assessed in the area of Aleppo, Syria (Al-Charideh, 2012) about 70 km east of the Amik Basin, but no evidence of their presence is available in the study area.

Among the sampled groundwaters, the hyperalkaline springs show the highest mean recharge altitude (1353–1768 m) indicating a hydrologic circulation that runs entirely within the ophiolitic complex.

Hyperalkaline and most of the shallow groundwaters plot very close to rainwater samples (Fig. 4) collected both in this study and in close-by areas (Yuce and Demirkol, 1990; Dirican et al., 2005; Yuce, 2005; Al-Charideh and Abou Zakhem, 2010; Al-Charideh, 2011) highlighting their recent meteoric origin. They are characterised, like all meteoric waters of the eastern Mediterranean area, by high deuterium excess values (d from 15.5 to 24.9‰) plotting close to the Eastern Mediterranean meteoric water line (EMMWL — Gat and Carmi, 1970). These high deuterium excess values (d > 10) are considered typical of a strong contribution of the Mediterranean Sea to atmospheric moisture in this

Table 4
Hydrogen and C_1–C_5 hydrocarbon contents and isotopic composition of Methane and Hydrogen. Sites in bold indicate free gas samples while the remaining indicate dissolved gas samples. nd = not determined.

Site	Date	H_2	C_1	C_2	C_3	C_4	C_5	$\delta^{13}C_{-CH_4}$	δD_{-CH_4}	δD_{-H_2}
	dd-mm-yyyy	ppm						‰	‰	‰
A4	04-08-2012	25.2	785,200	nd	nd	nd	nd	−65.5	nd	nd
A11	07-08-2012	13.6	863,200	nd	nd	nd	nd	−65.1	nd	nd
A23	05-08-2012	371,200	603,800	5118	1421	1407	1085	−5.6	−107	−749
A24	05-08-2012	384,200	607,400	5086	1387	1293	861	−5.1	−103	−762
A13	07-08-2012	487,400	102,500	24	11	16	12	−30.5	−326	−745
A12-2	28-06-2013	605,000	120,300	30	19	29	25	−30.4	−314	−712
A24-2	27-06-2013	379,800	602,900	5044	1359	1326	855	−4.8	−96	−704
A39	30-06-2013	35,000	288,600	nd	nd	nd	nd	−16.8	nd	nd

area (Gat and Carmi, 1970). Contrastingly, the waters collected from the deep wells are aligned along the mixing line between Eastern Mediterranean Sea Water and Local Meteoric Water (LMWL) (Fig. 4). Tritium is a radioactive isotope of hydrogen with half-life of 12.32 years useful in defining mean residence times of groundwater. It is produced steadily by cosmic rays in the upper stratosphere, but most of the tritium found in the environment was introduced during nuclear testing in the atmosphere in the early 1960s. The worldwide tritium contribution to rainwater recharge has been monitored through the Global Network of Isotopes in Precipitation of IAEA. Three of the monitoring stations of the network (Bet Dagan, Israel and Adana and Antalya, Turkey) are within a radius of 500 km from the study area and can be used to define the tritium deposition history in the study area. Most of the sampled groundwater displays tritium values not exceeding the present time rainwater recharge (~4–4.5 TU) and even the few samples (A1 and A2) reaching values up to 5.38 TU indicate a low contribution of waters recharged during the peak contribution of nuclear tritium. The wide range of tritium contents of the shallow groundwaters indicates great differences in mean residence times. On the contrary deep and hyperalkaline groundwaters have low to negligible tritium contents pointing to long mean residence times (>50 years). Quantification of the latter depends on the adopted hydrologic model (piston-flow or well-mixed model — Pearson and Truesdell, 1978). Hydrologic circuits perfectly reproducing a piston-flow model are rare and the only that could approximate it, in the study area, are those sampled from karstic springs (A2, A18 and A19). However, these springs show tritium values between 3.7 and 5.4 that, independently from the adopted model, indicate mean residence times of less than 50 a. The remaining groundwaters circulate in aquifers better approximated by the well-mixed model (Ozyurt, 2008). Longer mean residence times of some of them fit well with their increased ^{4}He contents and the, at least partial, attainment of equilibrium with the aquifer's rocks despite the low equilibration temperatures (see par. 5.3). In Fig. 5 the TDIC and $\delta^{13}C_{TDIC}$ values are reported along with the theoretical lines representing the TDIC and $\delta^{13}C_{TDIC}$ evolution of infiltrating water through carbonate terrains where CO_2 sources are active according to two different models: (i) addition of biogenic soil CO_2 deriving from oxidation of organic matter and root respiration ($\delta^{13}C$–CO_2org = −18 to −26‰) in equilibrium with calcite ($\delta^{13}C$–CO_2rock = 0‰) and (ii) addition of deeply derived CO_2. The curves were obtained by applying the geochemical modelling proposed by Chiodini et al. (2000). Infiltrating water has been assumed as local meteoric water initially in equilibrium with the atmosphere ($\delta^{13}C$–CO_2atm = −7‰). Almost all the shallow groundwater samples plot along the mixing curves between atmospheric and biogenic CO_2 evidencing a shallow origin for TDIC.

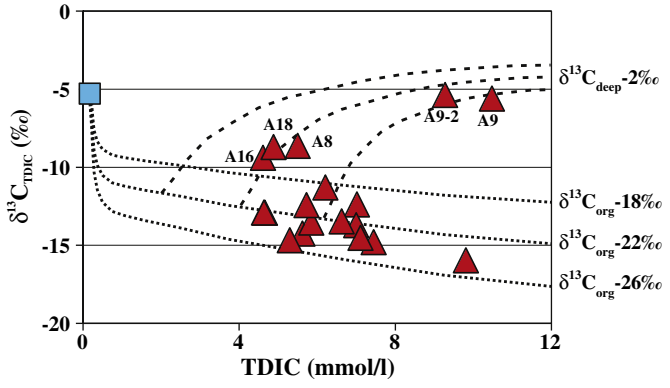

Fig. 5. TDIC (total dissolved inorganic carbon) contents vs. $\delta^{13}C_{TDIC}$ for the shallow groundwater samples. The same plot shows the theoretical curves of TDIC evolution obtained by applying the geochemical modelling proposed by Chiodini et al. (2000). Infiltrating water (pale blue square) has been assumed as local meteoric water initially in equilibrium with the atmosphere ($\delta^{13}C$–CO_2atm = −7‰). During infiltration (dotted lines) it interacts with organic CO_2, for which a range of the isotopic composition ($\delta^{13}C$–CO_2org = −18 ÷ −26‰) has been chosen. During this step, groundwater was also kept in equilibrium with calcite ($\delta^{13}C$ = 0‰). To take into account the samples lying above the dotted curves theoretical curves have been obtained by modelling the addition of a deep component having the Mediterranean magmatic CO_2 signatures ($\delta^{13}C$–CO_2 = −2 ± 2‰ Parks et al., 2013 and references therein; dashed lines). Three points having different initial TDIC contents (2, 4 and 6 mmol/l, respectively) have been chosen as starting values. (For interpretation of the references to colour in this figure legend, the reader is referred to the web version of this article.)

In contrast, the samples (A9 and A9-2) collected at one of the slightly thermalized groundwater sites lie clearly above these curves towards more positive $\delta^{13}C_{TDIC}$ values, thus pointing to the presence of a deeply-derived CO_2 enriched in heavy isotopes. Such process has been modelled taking into account a deep component having the Mediterranean magmatic CO_2 signatures ($\delta^{13}C$–CO_2 = −2 ± 2‰ – Parks et al., 2013 and references therein). Samples collected at A8, A16 and A18 show also a small but significant contribution of deeply-derived CO_2.

5.2. Gas geochemistry

About half of the samples show low N_2/O_2 ratios (4.9–7.1) close to the atmospheric ratio of 3.7 pointing to little or no consumption of oxygen by biologic or inorganic processes within the aquifer. Such processes can be invoked for the remaining samples showing ratios between 12 and 1524. The slightly thermalized samples are among those where oxygen consumption is more significant (Fig. 6a).

A mixture of atmospheric volatiles and others of different origin than the air is recognized to be a common feature where, CO_2, CH_4 and He may either originate from crustal-derived products, metasediments and hydrocarbon reservoirs, or from mantle-derived products as in the case of the basalts outcropping close to the Syrian borders.

The CH_4–CO_2–(N_2 + O_2) triangular diagram (Fig. 6b) shows the relationships between gas species typically representative of atmospheric (N_2 + O_2) and other sources (namely crust and mantle). The first main CO_2 reservoir for dissolved gas is the soil through meteoric recharge but during groundwater circulation many other crustal or/and mantle sources contribute to the CO_2 budget. Apart from the obvious CO_2-enrichment in volcanic areas, the venting of CO_2-rich waters is known to occur also over geothermal areas, well-known for their CO_2-rich thermal springs (e.g. Yellowstone, Wairakei or Larderello geothermal systems), tectonically active continental areas (e.g. NAF and EAF Zones, Turkey: Italiano et al., 2013), where CO_2-rich thermal waters bring a mixture of mantle-derived and metamorphic CO_2, or over the seismically active Central Apennines (Italy), where CO_2-rich springs carry gaseous CO_2 produced by mechano-chemical reactions (Italiano et al., 2008).

5.3. Gas–water interaction processes

The origin and the processes that regulate the CO_2 concentrations in the dissolved gases of the shallow groundwater samples of the Amik Basin can be constrained through their $\delta^{13}C_{TDIC}$ composition (Fig. 5) and their $CO_2/^3$He ratios (Fig. 7). These samples can be separated in two groups. The first group comprises most of the samples and their composition can be explained by simple addition of organic soil CO_2 all having low $\delta^{13}C_{TDIC}$ values and $CO_2/^3$He ratios much higher than that of atmospheric air (4.8×10^7).

The C-isotopic composition of the second group (Fig. 5) points to a significant addition of deep geogenic CO_2 of likely mantle origin. Nevertheless the $CO_2/^3$He ratios of these samples (Fig. 7), being much lower than that of the mantle (2×10^9, Marty and Jambon, 1987), indicate that these groundwaters lost CO_2 or/and acquired He. Due to the great difference in solubility of these two gases, the interaction of the deep deriving gas-phase with multilayered aquifers would bring to a preferential depletion of the most soluble gas during its travel towards the earth's surface. Therefore, the most soluble CO_2 will be progressively

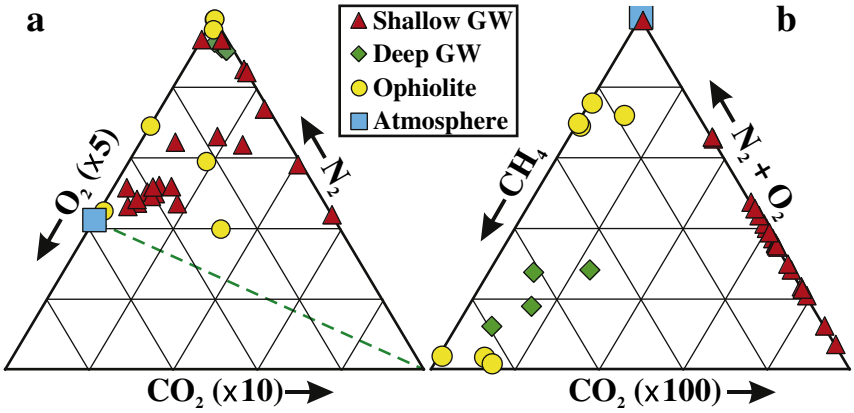

Fig. 6. (a) O_2–N_2–CO_2 and (b) CH_4–(O_2 + N_2)–CO_2 triangular plots. The green dashed line in (a) represents the O_2/N_2 ratio in atmospheric air. Ophiolite indicates samples collected from the hyperalkaline springs and from the dry gas seeps. (For interpretation of the references to colour in this figure legend, the reader is referred to the web version of this article.)

depleted due to dissolution, hydrolysis and possibly also carbonate precipitation processes while the less soluble He will be relatively enriched.

A strong CO_2 loss is also evident for the samples collected in the hyperalkaline springs and at the dry seeps (Fig. 7). As we will see in the following paragraphs this feature is typical of gases equilibrated in groundwater with deep circulation within serpentinized ultramafic rocks. Fig. 7 also confirms the ^4He enrichment of samples collected from the deep wells probably related to the addition of He- and CH_4-rich crustal fluids.

5.4. Water–rock interaction processes

The prevalent control on water chemistry in the shallow aquifers of the Amik basin is exerted by carbonate minerals. All these waters show saturation indexes within ±0.4 for calcite indicating that they are always close to saturation for this mineral. The widespread circulation within carbonate aquifers corroborates this result. Such finding also supports the decision of taking into account the equilibrium with carbonates in the modelling of the evolution of both TDIC and $\delta^{13}C_{TDIC}$ within the aquifers (Fig. 5).

For the same water samples, the saturation index for dolomite shows a slightly larger range with a few samples being undersaturated. The lowest values belong to slightly thermalized waters (A14 and A40 — SI = −1.27 and −0.95, respectively) where probably the Mg content

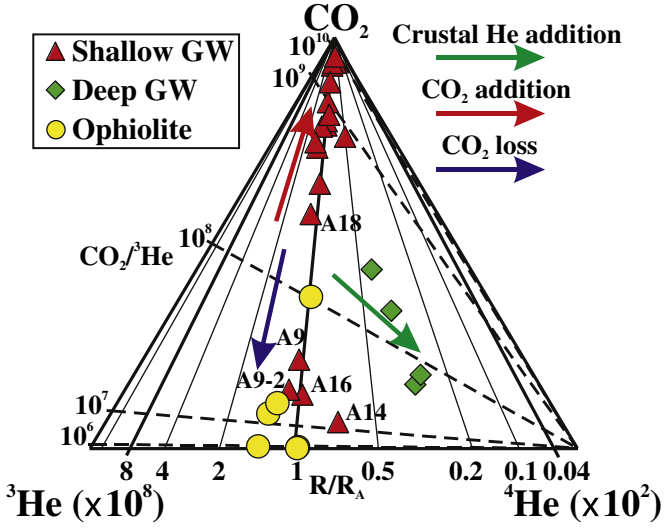

Fig. 7. CO_2–^3He–^4He triangular plot evidencing some of the main processes acting on the gases (free or dissolved) collected in the Amik Basin area.

has been lowered by precipitation of secondary minerals (Boschetti et al., 2013). This can be confirmed by the cation ternary plot (Fig. 8a — Giggenbach, 1988) where these two are the only shallow groundwaters plotting on the full equilibration curve (A14) or on partially equilibrated water field (A40) although pointing to low equilibration temperatures (<80 °C). Also the silica content does not evidence high temperature interactions. Silica concentrations show a large variability (9.5–69.1 mg/l) the lowest values being probably due to the limited presence of silicate phases within the aquifers (Fig. 8b). Anyway, all shallow groundwaters are undersaturated with respect to amorphous silica and oversaturated with respect to quartz, and possible equilibration tendency being probably masked by shallow mixing processes.

All deep groundwater samples plot also on the full equilibrium line in Fig. 8a indicating equilibration at low temperatures (<80 °C). As previously seen, these waters, together with the only fully equilibrated shallow groundwater, have very low or undetectable tritium contents pointing to slow and/or long hydrologic circuits. Low circulation velocities allow the attainment of chemical equilibrium even at low temperatures. This is also confirmed by the fact that the silica content of these waters seems to be in equilibrium with chalcedony (Fig. 8b). High temperature water–rock interaction process can also be excluded by the absence of any isotopic shift in the $\delta^{18}O$–δD plot (Fig. 4).

The very low silica content of the hyperalkaline waters, with saturation index well below that of quartz (Fig. 8b), is characteristic of the peculiar mineral assemblage of the ophiolitic rocks of their aquifers. In these aquifers, the silica content is rather controlled by reactions involving serpentine minerals. Furthermore, due to the peculiar mineralogy, the equilibrium attainment with the aquifer's rocks cannot be evaluated with the cation ternary plot of Giggenbach (1988) (Fig. 8a). Nevertheless, these waters are supposed to have reached equilibrium with the rocks. Their composition is, in fact, very similar to those found by Cipolli et al. (2004) in the serpentinite aquifers of the Gruppo di Voltri (Genova, Italy). The authors described the evolution of the groundwaters issuing from that ophiolitic complex through reaction path modelling and the composition of the hyperalkaline waters was obtained considering equilibration with the serpentinites under highly reducing closed-system conditions with respect to CO_2 (Cipolli et al., 2004).

5.5. Low-temperature serpentinization process

The above mentioned peculiar water–rock interaction process responsible of low-temperature serpentinization reactions is also the ideal environment for the production of H_2 and CH_4 (Suda et al., 2014). Both gases can be produced within ophiolitic rocks by several reactions both in low- and high-temperature environments (Etiope and Sherwood Lollar, 2013). All the gases collected in the hyperalkaline springs and at the dry gas seeps have high H_2 and CH_4 concentrations.

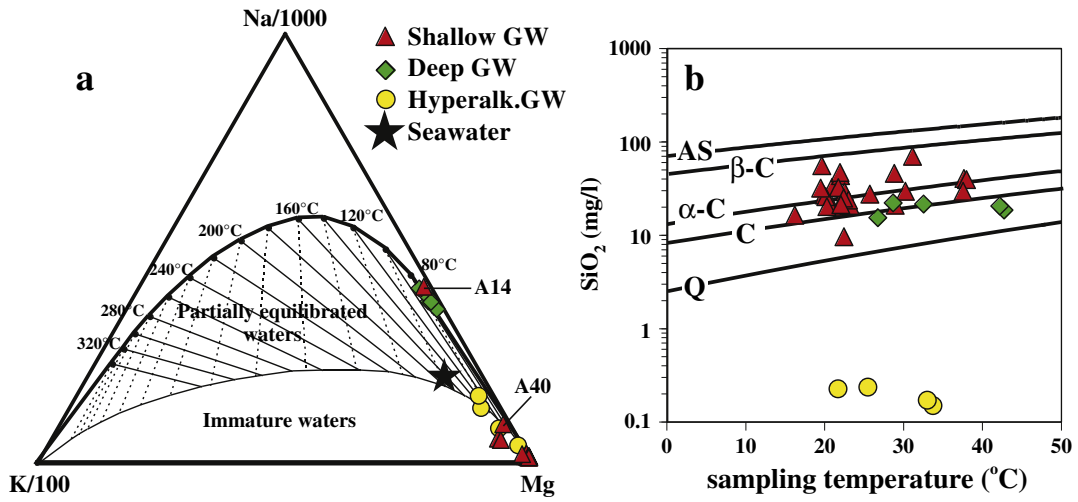

Fig. 8. (a) Na–K–$\sqrt{Mg}$ ternary diagram. The diagram provides information on the degree of water–rock equilibrium for low-temperature geothermal systems (Giggenbach, 1988). Although most of the sampled waters fall close to the Mg vertex, the plot allows for a clear distinction of the partially equilibrated thermal waters and the immature cold waters into well separated groups. Bold line indicates the full equilibrium line; the thin line indicates the boundary between immature and partially equilibrated waters. (b) Silica vs. sampling temperature binary diagram. Lines indicate equilibrium with different silica polymorphs (AS = amorphous silica; α-C and β-C = α- and β-cristobalite; C = chalcedony; Q = quartz).

Only the dissolved gas collected at site A35 shows no detectable H_2. The absence of H_2 at this site could have different explanations: a) methane formation without Hydrogen formation; b) hydrogen consumption within the deeper part of the aquifer through abiotic reactions; and c) biologic oxidation of Hydrogen at the spring outlet. All three hypotheses could apply to this site. The first process is thought to be favoured at low temperatures being linked to hydration reactions of olivine or orthopyroxene leading to serpentinization in the presence of a carbon source (Suda et al., 2014). The carbon source in the present case is represented by atmospheric and/or deep geogenic CO_2.

The second hypothesis relays on the fact that H_2 is generally abundantly produced in serpentinization processes and that CH_4 is consequently formed by Fisher–Tropsch-type reactions which consume the previously generated H_2 (Etiope and Sherwood Lollar, 2013). The inverse relation between the mean residence time (estimated through the tritium content considering a well-mixed reservoir model) and the H_2 concentration of the hyperalkaline springs could support this hypothesis. Spring A35 (Kisecik), with no detectable H_2 has a longer estimated mean residence time (TU = 0), with respect to spring A12 with H_2 concentrations up to 600,000 μmol/mol (TU = 1.64).

Finally, although microbial activity within hyperalkaline springs is generally very limited due to very low nutrient concentrations (Morrill et al., 2013), the biologic oxidation of H_2 at A35 could be favoured by the nearly stagnant conditions of this spring.

Further analyses will be necessary to better constrain the fate of H_2 in the hyperalkaline springs of the area. Nevertheless the isotopic composition of H_2 of both the dry seeps and the Tahtakopru spring samples gives us precious information about the environment in which it has been produced. The depleted δD–H_2 values are, in fact, similar to low-temperature seep sites in exposed sections of ancient oceanic crust such as the ophiolites in Oman, in Japan and in the submarine site of Lost City (Suda et al., 2014 and references therein). Using the isotopic geothermometer of Horibe and Craig (1995) between H_2 and H_2O, we obtain temperatures in the range from 15 to 56 °C for both Kurtbagi (sample A23) and Tahtakopru (sample A12). For the dry seep no data are available on δD–H_2O and therefore we select a value of −40‰, which is thought to represent the local groundwater and is about at the higher end of the values measured in the sampled hyperalkaline springs. Note that considering values of 0 or −80‰ would have changed the estimated temperatures of −6 or +6 °C. Using the isotope geothermometer of Bottinga (1969) that considers the equilibrium

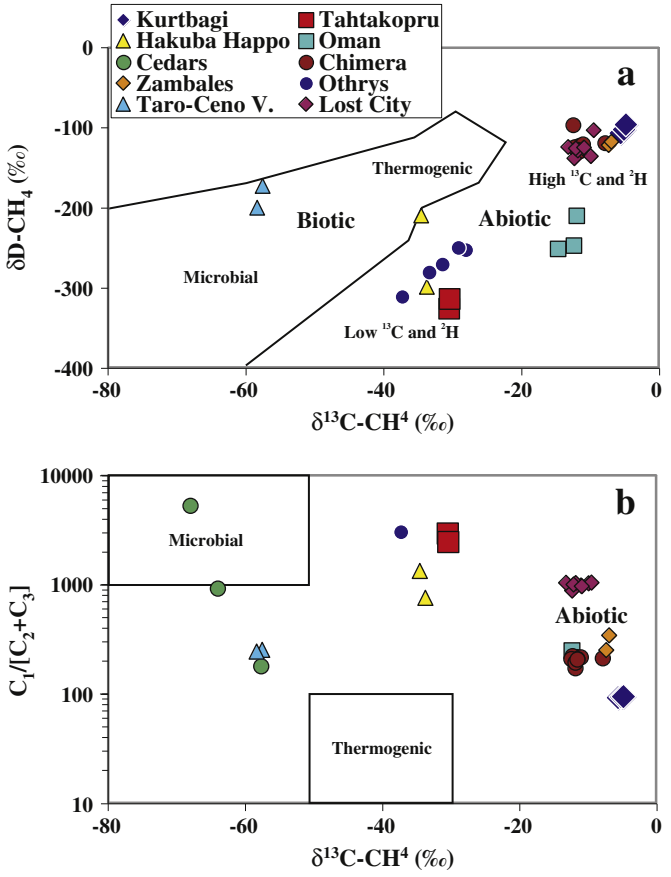

Fig. 9. (a) $\delta^{13}C$ vs. δD binary diagram of CH_4 and (b) $\delta^{13}C$–CH_4 vs. $C_1/[C_2 + C_3]$ ratio for the gases collected at the dry gas seeps of Kurtbagi and at the hyperalkaline spring of Tahtakopru compared with literature data from other serpentinized ultramafic rocks (Hakuba Happo — Japan, Suda et al., 2014; Oman, Fritz et al., 1992; Cedars — California, Morrill et al., 2013; Chimaera — Turkey, Etiope et al., 2011; Zambales — Philippines, Abrajano et al., 1988; Othrys — Greece, Etiope et al., 2013; Taro and Ceno Valleys — Italy, Boschetti et al., 2013; Lost City — Atlantic Ocean, Proskurowski et al. 2004 and 2006). In (a) the subdivision of the abiotic field in low and high $\delta^{13}C$ and $\delta^{2}H$ is made after Etiope and Sherwood Lollar (2013).

between CH_4 and H_2, the estimations of Kurtbagi and Tahtakopru, diverge somewhat. While the temperatures estimated at the dry seeps of Kurtbagi are similar (8–47 °C) to those estimated with the previous geothermometer, at Tahtakopru they are higher (83–113 °C). As we will see below this could depend on the fact that a part of the CH_4 found at Tahtakopru could be of biogenic origin and acquired after isotopic equilibration.

In Fig. 9a, the H- and C-isotopic compositions of CH_4 of our samples are plotted together with the data of CH_4 issuing from other ophiolitic complexes. The samples of the dry gas seeps (δD about −100‰ and δ^{13}C about −5‰) plot unambiguously in the abiotic CH_4 field with quite positive values. The samples of the hyperalkaline spring of Tahtakopru show instead much lighter values (δD about −320‰ and δ^{13}C about −30‰) and would have been classified until recent times as biotic (thermogenic), although recently Etiope and Sherwood Lollar (2013) suggested that the abiotic field could be extended including such values. The inclusion of the samples of Tahtakopru within this field, defined by the authors as ^{13}C–^{2}H-depleted abiotic gas field, would suggest an exclusive abiotic origin also for this gas. Nevertheless significant contributions of biotic CH_4 in gas samples issuing from ophiolitic complexes have been evidenced in other areas (Italy — Boschetti et al., 2013; California — Morrill et al., 2013) and they cannot be completely excluded also at Tahtakopru.

Also in Fig. 9b the samples collected at Tahtakopru spring plot far from those collected from the dry seeps and, having a much higher $C_1/[C_2 + C_3]$ ratio, they fall on a mixing line between a pure abiotic end-member and a microbial end-member further suggesting a contribution of some biogenic CH_4. Indeed some clues of hydrocarbon production in the area have been gathered in recent times (Ziegler, 2001) and also the samples we collected in the deep drillings of the Amik Basin show the abundant presence of CH_4 with a biotic C-isotopic composition (δ^{13}C–CH_4 of about −65‰).

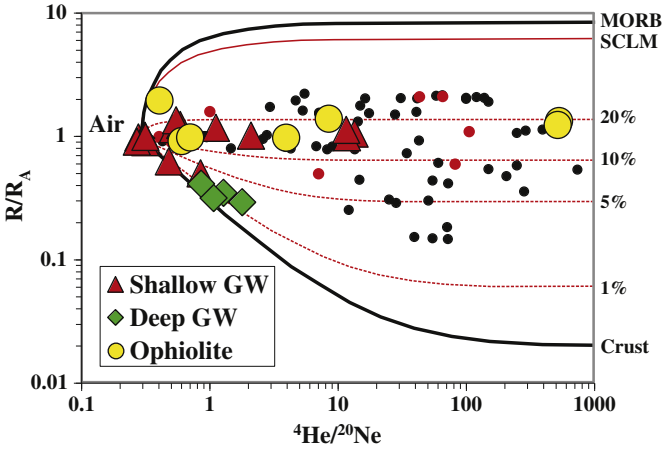

Fig. 10. Helium isotope signature of the collected samples. Data are superimposed on mixing curves (solid lines) of three end-member components, air, MORB and crust, for which the assumed typical values are as follows: MORB-type mantle $R/R_A = 8$ and SCLM mantle $R/R_A = 6.5$, $^4He/^{20}Ne > 1000$ (red line); crust $R/R_A = 0.02$ and $^4He/^{20}Ne > 1000$; air $R/R_A = 1$ and $^4He/^{20}Ne = 0.318$. Further air–crust mixing curves with 1, 5, 10 and 20% of SCLM mantle contribution have also been added (red stippled lines). Ophiolite indicates samples collected from the hyperalkaline springs and from the dry gas seeps. The error bars for helium isotopic measurements are within the symbol dimension. Samples shown by small dots (black — Torsfstein et al., 2013; red — Inguaggiato et al., in preparation) refer to data from the southern section of the DSF (from the Gulf of Aqaba to the Lake of Kinneret) and fall on the same range of our samples pointing to a widespread degassing of mantle-type volatiles along the whole DSF fault trace. (For interpretation of the references to colour in this figure legend, the reader is referred to the web version of this article.)

5.6. He isotopic signature and tectonic setting

A very useful geochemical tool to constrain the involved gas sources is the isotopic ratio of helium due the possibility of defining its origin. Helium and its isotopes are excellent natural tracers of mantle–crust interactions in different geotectonic provinces because of their chemical inertness and the negligible isotopic fractionation during gas–water–rock interaction processes. Distinct mantle, crustal, and atmospheric helium sources are characterised by well-defined isotopic compositions, constraining also the volatiles' genesis and history. Helium from the continental crust with negligible addition of mantle volatiles has low $^3He/^4He$ ratios in the range of 0.01–0.05 R_A, reflecting a strong radiogenic ^{4}He component. The upper asthenosphere, as constrained by samples of mid-ocean ridge basalt (MORB), has a $^3He/^4He$ ratio of 8 ± 1 R_A (Ballentine et al., 2002) indicating the presence of primordial ^{3}He acquired during the Earth's formation.

The R/R_A–$^4He/^{20}Ne$ graph of Fig. 10 shows two distinct trends depicted by the majority of the samples while some of the shallow groundwaters plot close to the atmospheric end-member (air, Fig. 10). One trend, including the deep groundwaters and two shallow groundwaters (A25 and A40), fall along a mixing line between air and an almost pure crustal end-member. The other trend is drawn by the samples collected at the hyperalkaline springs and the dry seeps as well as the most He-enriched shallow groundwater samples and defines a mixing line between air and an end-member of prevailing crustal origin with a significant contribution (10–20%) of mantle-derived helium.

The presence of a significant mantle He signature has often been used to track the input of mantle fluids in the crust either through the injection of magma batches (Sano and Wakita, 1985; Allard et al., 1997; Italiano et al., 2000) or along deep-rooted regional transform faults. Examples of the latter mechanism have already been found in Turkey along the NAF (Gülec et al., 2002) and the EAF (Italiano et al., 2013), in Greece (D'Alessandro et al., 2014), in California at the San Andreas Fault (Kulongoski et al., 2013), in Himalaya at the Karakoram Fault (Klemperer et al., 2013) and along the DSF in Israel (Torfstein et al., 2013). In addition, helium isotopes in dissolved and free gases may be an important geochemical indicator of seismic and tectonic activity (Kennedy and van Soest, 2007; Umeda et al., 2008; Italiano et al., 2009b; de Leeuw et al., 2010). Considering the contemporary presence of active faults (along the DSF) and recent basaltic outcrops (Fig. 2) marking the Amik Basin, the measured $^3He/^4He$ ratios are relatively low, and always lower than those measured southerly along the DSF (Torfstein et al., 2013). Therefore a consistent contribution of a crustal ^{4}He-rich source has to be considered. In order to estimate the relative contribution of helium from the three main sources (air, mantle and crust) we adopted the following equations (Sano and Wakita, 1985):

$$\left(^3He/^4He\right) = \left(^3He/^4He\right)_M \times M + \left(^3He/^4He\right)_C \times C + \left(^3He/^4He\right)_A \times A$$
$$1/\left(^4He/^{20}Ne\right) = M/\left(^4He/^{20}Ne\right)_M + C/\left(^4He/^{20}Ne\right)_C + A/\left(^4He/^{20}Ne\right)_A$$
$$M + C + A = 1$$

where M, C and A represent the fractions of mantle, continental crust and atmospheric helium, respectively. The end-members used in the present calculation were:

$$\left(^3He/^4He\right)_M = 6.5R_A;\ \left(^4He/^{20}Ne\right)_M \geq 1000;$$
$$\left(^3He/^4He\right)_C = 0.02R_A;\ \left(^4He/^{20}Ne\right)_C \geq 1000;$$
$$\left(^3He/^4He\right)_A = 1R_A;\ \left(^4He/^{20}Ne\right)_A = 0.318$$

for free gases and 0.268 for dissolved gases (Holocher et al., 2002).

Instead of the generally used MORB-type mantle, we used a SCLM-type mantle as our end-member. There is a great deal of evidence supporting such an end-member in the European and Mediterranean

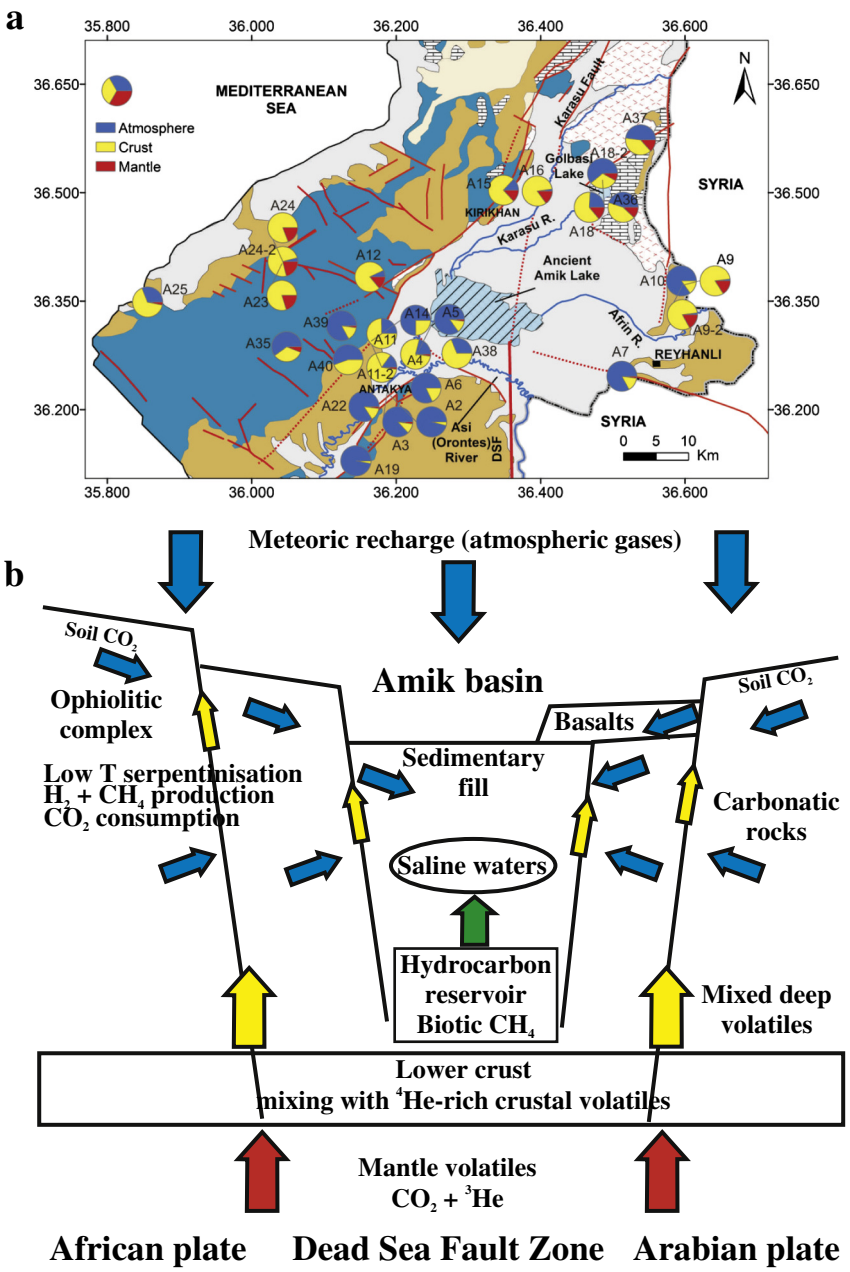

Fig. 11. (a) Map showing the relative contribution of atmospheric, crustal and mantle components to the total He in the samples collected in the study area. (b) Schematic fluid circulation model of the study area. The blue arrows indicate the groundwater circulation, the red arrows the mantle volatile supply, the green arrow the hydrocarbon reservoir within the sedimentary sequence of the Amik Basin and the yellow arrows evidence the upflow along deep-rooted faults of deep circulating fluids enriched in deep volatiles (mantle and crustal) or/and fluids originating from low temperature serpentinization processes. (For interpretation of the references to colour in this figure legend, the reader is referred to the web version of this article.)

area (Dunai and Baur, 1995; Gautheron et al., 2005; Shimizu et al., 2005; Torfstein et al., 2013) with estimated values ranging from 6.2 to 6.5. The end-member value used in the present calculations (6.5 R_A) is that estimated for the Eastern Mediterranean area by Torfstein et al. (2013).

The estimated contributions of the three components are shown in Table 3 and, graphically, in Fig. 11a. Also in this case three groups can be recognised. The first group shows a large atmospheric component (generally >75%) and is composed of samples from the "shallow groundwater" group (A2, A3, A5, A6, A7, A10, A14, A19, A22 and A40). Those samples were collected almost exclusively along the southern margin of the Amik Basin and along the Antakya graben (Fig. 11a). Such a large atmospheric contribution is probably due to the huge meteoric recharge and relatively rapid karstic circulation in this area, probably masking the deep contribution, if any. A different explanation is given for two of the hyperalkaline springs (A35 and A39) having also a prevailing atmospheric contribution due to air dissolution in the nearly stagnant waters at the spring mouth as a consequence of the very low water flow rate.

The second group of samples is represented by samples with a prevailing crustal contribution and negligible mantle contribution (<3%). This group is made of all the deep groundwaters from the thick sedimentary sequence within the Amik Basin and the only shallow groundwater (A25) collected close to the Mediterranean coast, far away the Amik Basin (Fig. 11a). These samples referring to aquifers with slow circulation have been enriched in CH_4- or N_2-dominant crustal fluids.

The last group composed of samples collected at the dry gas seeps of Kurtbagi (A23) and the hyperalkaline spring of Tahtakopru (A12) and some of the shallow groundwaters (A9, A15, A16, A18, A36 and A37) with a prevailing crustal component, display a significant contribution

of mantle-derived helium (8–21%) and low air contamination. Moreover, considering the atmospheric component of the hyperalkaline springs A35 and A39 as a shallow and local contamination process, also these samples could belong to this group. Furthermore, it is worth of notice that, among the shallow groundwaters, samples showing a distinct deep CO_2 contribution (namely A9, A16, A18; Fig. 5) belong to this group. The estimated mantle-helium percentages in the mixture refer to a SCLM-type helium end-member. In our case, however the possibility that the helium nowadays degassed over the eastern area (e.g. samples 9 and 18) is isotopically fractionated due to the faster degassing rate of the lower helium mass degassing from relatively small magma bodies.

Most of the samples of the third group come from the northern part of the Amik Basin at the conjunction with the Karasu Basin. This area is characterised by the presence of various tectonic structures linked to the Karasu Fault and the DSF Systems, and also by the outcrop of the Quaternary Basalts (Fig. 11a). The remaining samples have been collected within the ophiolitic complex generally close to important tectonic structures (Fig. 11a).

As shown in Fig. 11a, helium in the collected volatiles can be considered as a mixture at variable extents between a crustal, ^{4}He-rich, and a mantle-derived source. Based on our results, this is irrespective of the location of the samples on the African or Arabian plates. It is easy to observe that the ^{3}He source could be identified in the volcanic systems recently active on the Arabian Plate; however we have no volcanoes on the western margin of the basin (African plate). Therefore, we suggest that the DSF zone plays the main role on the western part of the basin allowing the uprising of CO_2-dominated, mantle-type volatiles and the release of ^{4}He trapped in buried crustal blocks. Such a mixing of a prevailing crustal component with mantle gases has been evidenced also along other sections of the DSF (Torfstein et al., 2013). In our case the mantle/crust mixing ratio has a rather narrow range (15–20% mantle; Fig. 10), while southerly (Torfstein et al., 2013) it spans from a 3 to 36% (Fig. 10). Torfstein et al. (2013) proposed a variable input of the mantle component on a constant crustal flux as a consequence of changes in the lithosphere conditions, e.g. a thinner crust and more developed fracture system towards the north (Lake Kinneret area), with respect to the southern area (Arava Valley). The almost homogeneous distribution of the mantle-derived helium component in the DSF segment crossing the Amik Basin could be related to the short length of the Hatay fault segment (<100 km), considered in the present study, compared to the area investigated by Torfstein et al. (2013) (about 300 km).

This model can be considered as reliable for the African Plate (western side) while on the Arabian plate the main source of ^{3}He could be found in the recent emplacements of mafic rocks. Although there is no evidence that an active magmatic degassing occurs, the recent magmatic activity (dated as young as 50 ka — Çapan et al., 1987; Rojay et al., 2001) is able to supply mantle-type volatiles during the cooling down of buried magmatic bodies.

The main question, however, is where the large amount of ^{4}He comes from. Although it is possible that some oil reservoirs recognized over the study area (Ziegler, 2001) release large amounts of radiogenic helium, it is unlikely that the oil reservoirs could be the responsible for a regional ^{4}He degassing as the distribution of the recorded helium isotopic data highlights. The answer instead should be found in the large-scale tectonic settings of the whole area, including the Arabian, African and Anatolian collision areas, also responsible for the genesis and emplacement of the ophiolitic blocks (e.g. Yilmaz et al., 1993; Robertson, 2002). Crustal helium is most likely degassed by the remnants of metamorphic or flyshoid rocks involved in ophiolite obduction at relatively shallow depths (a few kilometres) and by the crystalline basement located at deeper crustal levels down to the Moho transition estimated to be relatively shallow in the area (about 30 km — Vanacore et al., 2013; Tezel et al., 2013). We propose that the regional degassing over that large area occurs because the deep mantle-type volatiles reach the surface moving across the shallow levels fracture field of the active DSF. On their way to the surface the mantle volatiles mix with crustal fluids, allowing and probably also enhancing the release of radiogenic helium.

6. Conclusions

The complex geodynamic setting of the Amik Basin, which is located at the boundary between three tectonic plates, is reflected in the large compositional range of the collected fluids. Fig. 11b shows a schematic circulation model that summarizes the three main factors controlling origin and evolution of the fluids: hydrology, composition of the aquifers' rocks and main tectonic structures. The first factor discriminates between shallow and deep hydrologic circuits. The shallow aquifers are characterised by low salinity waters and a dissolved gas phase composed of a mixture of atmospheric and CO_2-dominated gases. The groundwaters marked by deep and slow circulation display a large compositional variety in the chemical and isotopic composition of both waters (from low to very high salinity) and dissolved gases. All of the deep ground waters display clues of deep sourced fluids inputs either of crustal or mantle origin, irrespectively of their location on the African or Arabian Plates.

The influence of the aquifers' rock composition is evident in the Ca–HCO_3 composition of most of the shallow groundwaters circulating in carbonate rocks. Contrastingly, the geochemical features of the samples collected from the deep wells within the Amik Basin is strongly influenced by the connate water and organic content of the recent marine sediments that fill up the basin. The high salinity of these waters is, in fact, justified by mixing with a seawater end-member and the high dissolved CH_4 probably comes from hydrocarbon reservoirs deeply buried within the thick sedimentary sequence of the Amik Basin. The most impressive control of the aquifers rocks, however, is found in the fluids collected in the ophiolitic complex were hyperalkaline waters with a peculiar Ca–OH composition and H_2- and CH_4-rich gases have been found.

The geochemical features of the gas released over the whole study area highlight mixings at variable extents of gas species coming from air, crust and mantle sources. The CO_2-enriched gases dissolved in shallow groundwaters show sometimes helium isotopic ratios with a significant mantle contribution consistent with the presence of recently emplaced basalts. The deep groundwaters (from boreholes deeper than 1000 m) have a CH_4-dominated dissolved gas phase related to the presence of hydrocarbon reservoirs. Their ^{3}He/^{4}He ratios, lower than those of the other gases, are consistent with the radiogenic-type helium normally associated to hydrocarbons.

The ophiolite block located in westernmost area of the basin, is marked by the H_2-dominated gases with abiogenic methane. All of the gases collected from the ophiolites (both gas seepage and dissolved gases) carry variable contents of mantle-derived fluids as shown by the measured helium isotopic ratio. In our opinion, the deep, mantle-type volatiles do not contribute to the serpentinization process and thus is not responsible for the production of abiogenic methane and H_2. We propose that the serpentinization occurs because of the alteration at relatively low pressure and temperature of the deeper portions of the ophiolitic complex.

The widespread presence of CO_2 testifies a regional degassing activity although the soil degassing over the Amik Basin area is not particularly anomalous (Yuce et al., in prep.). This might be due to two main, sometimes concomitant, causes: CO_2 dissolution and hydrolysis due to the huge groundwater circulation and CO_2 consumption by low temperature serpentinization of the mafic and ultramafic rocks of the ophiolitic complex. The presence of a multilayered aquifer system in the Amik Basin enhances the CO_2 dissolution process. Furthermore, the presence of thick ophiolitic sequences beneath the sedimentary layers in parts of the same basin (Hacimehmetoglu and Cicek, personal communication) could act as CO_2 sink also outside the area in which the ophiolitic sequence crops out.

Finally, the tectonics of the area and the influence of the main tectonic structures can be recognized both in the diffuse presence of CO_2 associated to a significant contribution of mantle-derived fluids (see samples collected on the north-eastern and western margins of the Amik Basin) superimposed to the regional degassing of crustal-type helium. The absence of recent volcanism and the presence of the DSF and the Karasu Fault systems over the Hatay Province, points to a degassing of deep-originated volatiles enhanced by the lithospheric character of the two fault systems. The variety and complexity of the geochemical features of the fluids collected over the Amik Basin coherently fit the complex, maybe unique, geodynamic setting of the area at the boundaries of three tectonic plates.

Acknowledgements

This work has been funded by the Scientific and Technological Research Council of Turkey (TUBITAK) with the project (COST) no. 111Y090. The authors wish to thank Fausto Grassa, Mauro Martelli, Ygor Oliveri, Andrea Rizzo, Francesco Salerno, Aldo Sollami and Mariano Tantillo for their kind and valuable support in gas analyses. Gokhan Hacimehmetoglu from TPAO and Aydin Cicek from MTA are kindly acknowledged for the stratigraphic data of Amik Basin boreholes. The comments and suggestions of two anonymous referees and of the Editor David Hilton helped us improve the manuscript.

References

Abrajano, T.A., Sturchio, N.C., Bohlke, J.K., Lyon, G.L., Poreda, R.J., Stevens, C.M., 1988. Methane-hydrogen gas seeps, Zambales Ophiolite, Philippines: deep or shallow origin? Chem. Geol. 71, 211–222.

Akyüz, H.S., Altunel, E., Karabacak, V., Yalçıner, C.Ç., 2006. Historical earthquake activity of the northern part of the Dead Sea Fault zone, southern Turkey. Tectonophysics 426, 281–293.

Alchalbi, A., Daoud, M., Gomez, F., McClusky, S., Reilinger, R., Abu Romeyeh, M., Alsouod, A., Yassminh, R., Ballani, B., Darawcheh, R., Sbeinati, R., Radwan, Y., Al Masri, Y., Bayerly, M., Al Ghazzi, R., Barazangi, M., 2010. Crustal deformation in northwestern Arabia from GPS measurements in Syria: slow slip rate along the northern Dead Sea Fault. Geophys. J. Int. 180, 125–135. http://dx.doi.org/10.1111/j.1365-246X.2009.04431.x.

Al-Charideh, A., 2011. Environmental isotope study of groundwater discharge from the large karst springs in West Syria: a case study of Figeh and Al-sin springs. Environ. Earth Sci. 63, 1–10. http://dx.doi.org/10.1007/s12665-010-0660-x.

Al-Charideh, A., 2012. Geochemical and isotopic characterization of groundwater from shallow and deep limestone aquifers system of Aleppo basin (north Syria). Environ. Earth Sci. 65, 1157–1168. http://dx.doi.org/10.1007/s12665-011-1364-6.

Al-Charideh, A., Abou Zakhem, B., 2010. Distribution of tritium and stable isotopes in precipitation in Syria. Hydrol. Sci. J. 55 (5), 832–843. http://dx.doi.org/10.1080/02626667.2010.487977.

Allard, P., Jean-Baptiste, P., D'Alessandro, W., Parello, F., Parisi, B., Flehoc, C., 1997. Mantle-derived helium and carbon in groundwaters and gases of Mount Etna, Italy. Earth Planet. Sci. Lett. 148, 501–516.

Al-Momani, I.F., Tuncel, S., Eler, U., Ortel, E., Sirin, G., Tuncel, G., 1995. Major ion composition of wet and dry deposition in eastern Mediterranean basin. Sci. Total Environ. 164, 75–85.

Altunel, E., Meghraoui, M., Karabacak, V., Akyüz, S., Ferry, M., Yalçıner, Ç., Munschy, M., 2009. Archaeological sites (Tell and Road) offset by the Dead Sea Fault in the Amik Basin, Southern Turkey. Geophys. J. Int. 179, 1313–1329.

Ballentine, C.J., Burgess, R., Marty, B., 2002. Tracing fluid origin, transport and interaction in the crust. Rev. Mineral. Geochem. 47, 539–614. http://dx.doi.org/10.2138/rmg.2002.47.13.

Barka, A., Reilinger, R., 1997. Active tectonics of the Mediterranean region: deduced from GPS, neotectonic and seismicity data. Ann. Geofis. XI/3, 587–610.

Bellomo, S., D'Alessandro, W., Longo, M., 2003. Volcanogenic fluorine in rainwater around active degassing volcanoes: Mt. Etna and Stromboli Island, Italy. Sci. Total Environ. 301, 175–185. http://dx.doi.org/10.1016/S0048-9697(02)00284-X.

Boschetti, T., Etiope, G., Pennisi, M., Romain, M., Toscani, L., 2013. Boron, lithium and methane isotope composition of hyperalkaline waters (Northern Apennines, Italy): terrestrial serpentinization or mixing with brine? Appl. Geochem. 32, 17–25. http://dx.doi.org/10.1016/j.apgeochem.2012.08.018.

Bottinga, Y., 1969. Calculated fractionation factors for carbon and hydrogen isotope exchange in the system calcite–carbon dioxide–graphite–methane–hydrogen–water vapor. Geochim. Cosmochim. Acta 33 (1), 49–64.

Boulton, S., Robertson, A.H.F., 2008. The Neogene–Recent Hatay Graben, South Central Turkey: graben formation in a setting of oblique extension (transtension) related to post-collisional tectonic escape. Geol. Mag. 145, 800–821. http://dx.doi.org/10.1017/S0016756808005013.

Boulton, S., Robertson, A.H.F., Ünlügenç, U.C., 2006. Tectonic and sedimentary evolution of the Cenozoic Hatay Graben, Southern Turkey: a two-phase model for graben formation. In: Robertson, A.H.F., Mountrakis, D. (Eds.), Tectonic Development of the Eastern Mediterranean Region. Geol. Soc. London Spec. Publ. 260, pp. 613–634. http://dx.doi.org/10.1144/GSL.SP.2006.260.01.26.

Çapan, U.Z., Vidal, P., Cantagrel, J.M., 1987. K–Ar, Nd, Sr and Pb isotopic study of the Quaternary volcanism in Karasu Rift (Hatay), N-end of Dead Sea rift zone in SE Turkey. H.Ü. Yerbilimleri 14, 165–178.

Capasso, G., Favara, R., Grassa, F., Inguaggiato, S., Longo, M., 2005. On-line technique for preparation and measuring stable carbon isotope of total dissolved inorganic carbon in water samples ($\delta^{13}C_{TDIC}$). Ann. Geophys. 48, 159–166. http://dx.doi.org/10.4401/ag-3190.

Chaimov, T.A., Barazangi, M., 1990. Crustal shortening in the Palmyride Fold Belt, Syria, and implications for movement along Dead Sea fault system. Tectonics 9, 1369–1386.

Chiodini, G., Frondini, F., Cardellini, C., Parello, F., Peruzzi, L., 2000. Rate of diffuse carbon dioxide Earth degassing estimated from carbon balance of regional aquifers: the case of central Apennine, Italy. J. Geophys. Res. 105, 8423–8434.

Cipolli, F., Gambardella, B., Marini, L., Ottonello, G., Zuccolini, M.V., 2004. Geochemistry of high-pH waters from serpentinites of the Gruppo di Voltri (Genova, Italy) and reaction path modeling of CO_2 sequestration in serpentinite aquifers. Appl. Geochem. 19, 787–802. http://dx.doi.org/10.1016/j.apgeochem.2003.10.007.

Craig, H., 1961. Isotopic variations in meteoric waters. Science 133, 1702–1703.

D'Alessandro, W., Katsanou, K., Lambrakis, N., Bellomo, S., Brusca, L., Liotta, M., 2013. Chemical and isotopic characterisation of bulk deposition in the Louros Basin (Epirus, Greece). Atmos. Res. 132–133, 399–410. http://dx.doi.org/10.1016/j.atmosres.2013.07. 007.

D'Alessandro, W., Brusca, L., Kyriakopoulos, K., Bellomo, S., Calabrese, S., 2014. A geochemical traverse along the "Sperchios Basin — Evoikos Gulf" Graben (Central Greece): origin and evolution of the emitted fluids. Mar. Pet. Geol. http://dx.doi.org/10.1016/j.marpetgeo.2013.12.011.

D'Alessandro, W., Federico, C., Longo, M., Parello, F., 2004. Oxygen isotope composition of natural waters in the Mt. Etna area. J. Hydrol. 296, 282–299. http://dx.doi.org/10.1016/j.jhydrol.2004.04.002.

de Leeuw, G.A.M., Hilton, D.R., Güleç, N., Mutlu, H., 2010. Regional and temporal variations in $CO_2/^3He$, $^3He/^4He$ and $\delta^{13}C$ along the North Anatolian fault zone, Turkey. Appl. Geochem. 25, 524–539. http://dx.doi.org/10.1016/j.apgeochem.2010.01.010.

Dilek, Y., Thy, P., 2009. Island arc tholeiite to boninitic melt evolution of the Cretaceous Kizildag (Turkey) ophiolite: model for multi-stage early arc–forearc magmatism in Tethyan subduction factories. Lithos 113, 68–87. http://dx.doi.org/10.1016/j.lithos.2009.05.044.

Dirican, A., Ünal, S., Acar, Y., Demircan, M., 2005. The temporal and seasonal variation of H-2 and O-18 in atmospheric water vapour and precipitation from Ankara, Turkey in relation to air mass trajectories at Mediterranean Basin. Isotopic Composition of Precipitation in the Mediterranean Basin in Relation to Air Circulation Patterns and Climate. IAEA, Vienna, pp. 191–214 (IAEA-TECDOC-1453).

Dunai, T.J., Baur, H., 1995. Helium, neon, and argon systematics of the European subcontinental mantle: implications for its geochemical evolution. Geochim. Cosmochim. Acta 59, 2767–2783.

Erdik, M., Aydinoglu, N., Pinar, A., Kalafat, D., 1997. Hatay Deprem Raporu. Kandilli Obs, Istanbul.

Etiope, G., Sherwood Lollar, B., 2013. Abiotic methane on Earth. Rev. Geophys. 51, 276–299. http://dx.doi.org/10.1002/rog.20011.

Etiope, G., Schoell, M., Hosgörmez, H., 2011. Abiotic methane flux from the Chimaera seep and Tekirova ophiolites (Turkey): understanding gas exhalation from low temperature serpentinization and implications for Mars. Earth Planet. Sci. Lett. 310, 96–104. http://dx.doi.org/10.1016/j.epsl.2011.08.001.

Etiope, G., Tsikouras, B., Kordella, S., Ifandi, E., Christodoulou, D., Papatheodorou, G., 2013. Methane flux and origin in the Othrys ophiolite hyperalkaline springs, Greece. Chem. Geol. 347, 161–174. http://dx.doi.org/10.1016/j.chemgeo.2013.04.003.

Freund, R., Zak, I., Garfunfel, Z., 1968. On the age and rate of sinistral movement along the Dead Sea rift. Nature 220, 253–255.

Fritz, P., Clark, I.D., Fontes, J.C., Whiticar, M.J., Faber, E., 1992. Deuterium and ^{13}C evidence for low-temperature production of hydrogen and methane in a highly alkaline groundwater environment in Oman. In: Kharaka, Y.K., Maest, A.S. (Eds.), Proc. 7th Internat. Symp. Water–Rock Interaction. A.A. Balkema, Rotterdam, pp. 793–796.

Garfunkel, Z., 1981. Internal structure of the Dead Sea leaky transform (rift) in relation to plate kinematics. Tectonophysics 80, 81–108.

Garfunkel, Z., Zak, I., Freund, R., 1981. Active faulting in the Dead Sea rift. Tectonophysics 80, 1–26.

Gat, J.R., Carmi, I., 1970. Evolution of the isotopic composition of the atmospheric water in the Mediterranean Sea area. J. Geophys. Res. 75, 3039–3048.

Gautheron, C., Moreira, M., Allegre, C., 2005. He, Ne and Ar composition of the European lithospheric mantle. Chem. Geol. 217, 97–112. http://dx.doi.org/10.1016/j.chemgeo.2004.12.009.

Giggenbach, W.F., 1988. Geothermal solute equilibria. Derivation of Na–K–Mg–Ca geoindicators. Geochim. Cosmochim. Acta 52, 2149–2765.

Gomez, F., Karam, G., Khawlie, M., McClusky, S., Vernant, P., Reilinger, R., Jaafar, R., Tabet, C., Khair, K., Barazangi, M., 2007. Global positioning system measurements of strain accumulation and slip transfer through the restraining bend along the Dead Sea fault system in Lebanon. Geophys. J. Int. 168, 1021–1028.

Gülec, N., Hilton, D.R., Mutlu, H., 2002. Helium isotope variations in Turkey: relationship to tectonics, volcanism and recent seismic activities. Chem. Geol. 187, 129–142.

Hempton, M.R., 1987. Constraints on Arabian plate motion and extensional history of the Red Sea. Tectonics 6, 687–705.

Holocher, J., Peeters, F., Aeschbach-Hertig, W., Hofer, M., Brennwald, M., Kinzelbach, W., Kipfer, R., 2002. Experimental investigations on the formation of excess air in quasi-saturated porous media. Geochim. Cosmochim. Acta 66 (23), 4103–4117.
Horibe, Y., Craig, H., 1995. D/H fractionation in the system methane–hydrogen–water. Geochim. Cosmochim. Acta 59 (24), 5209–5217.
Inguaggiato, S., Rizzo, A., 2004. Dissolved helium isotope ratios in groundwaters: a new technique based on gas–water re-equilibration and its application to Stromboli volcanic system. Appl. Geochem. 19, 665–673. http://dx.doi.org/10.1016/j.apgeochem.2003.10.009.
Italiano, F., Martelli, M., Martinelli, G., Nuccio, P.M., 2000. Geochemical evidences of melt intrusions along lithospheric faults of Irpinian Apennines (Southern Italy): geodynamic and seismogenetic implications. J. Geophys. Res. 105 (B6), 13569–13578.
Italiano, F., Martinelli, G., Plescia, P., 2008. CO_2 degassing over seismic areas: the role of mechanochemical production at the study case of Central Apennines. Pageoph 165 (1), 75–94. http://dx.doi.org/10.1007/s00024-007-0291-7.
Italiano, F., Bonfanti, P., Ditta, M., Petrini, R., Slejko, F., 2009a. Helium and carbon isotopes in the dissolved gases of Friuli region (NE Italy): geochemical evidence of CO_2 production and degassing over a seismically active area. Chem. Geol. 266, 76–85. http://dx.doi.org/10.1016/j.chemgeo.2009.05.022.
Italiano, F., Martinella, G., Bonfanti, P., Caracausi, A., 2009b. Long-term geochemical monitoring of gases from the seismic area of the Umbria region: 1997–2007. Tectonophysics 476, 282–296. http://dx.doi.org/10.1016/j.tecto.2009.02.040.
Italiano, F., Sasmaz, A., Yuce, G., Okan, O.O., 2013. Thermal fluids along the East Anatolian Fault Zone (EAFZ): geochemical features and relationships with the tectonic setting. Chem. Geol. 339, 103–114. http://dx.doi.org/10.1016/j.chemgeo.2012.07.027.
Italiano, F., Yuce, G., Uysal, I.T., Gasparon, M., Morelli, G., 2014. Insights into mantle-type volatiles contribution from dissolved gases in artesian waters of the Great Artesian Basin, Australia. Chem. Geol. 378-379, 75–88.
Karabacak, V., Altunel, E., 2013. Evolution of the northern Dead Sea fault zone in southern Turkey. J. Geodyn. 65, 282–291.
Karabacak, V., Altunel, E., Meghraoui, M., Akyüz, H.S., 2010. Field evidences from northern Dead Sea fault zone (South Turkey): new findings for the initiation age and slip rate. Tectonophysics 480, 172–182.
Kasapoglu, E.K., 1987. Seismotectonic characteristics of Eastern Mediterranean: a finite elements analysis. H.Ü. Yerbilimleri 14, 309–317.
Kennedy, B.M., van Soest, M.C., 2007. Flow of mantle fluids through the ductile lower crust: helium isotope trends. Science 318, 1433–1436. http://dx.doi.org/10.1126/science.1147537.
Kiratzi, A.A., 1993. A study of the active crustal deformation of the North and East Anatolian fault zones. Tectonophysics 225, 191–203.
Klemperer, S.L., Kennedy, B.M., Sastry, S.R., Makovsky, Y., Harinarayana, T., Leech, M.L., 2013. Mantle fluids in the Karakoram fault: helium isotope evidence. Earth Planet. Sci. Lett. 366, 59–70. http://dx.doi.org/10.1016/j.epsl.2013.01.013.
Kulongoski, J.T., Hilton, D.R., Barry, P.H., Esser, B.K., Hillegonds, D., Belitz, K., 2013. Volatile fluxes through the Big Bend section of the San Andreas Fault, California: helium and carbon-dioxide systematics. Chem. Geol. 339, 92–102. http://dx.doi.org/10.1016/j.chemgeo.2012.09.007.
Kuran, U., 1980. The location, magnitude and long-term time prediction of damaging earthquakes along the Anatolian faults and Levant coast. Bull. Geol. Congress of Turkey 2, pp. 151–163.
Le Beon, M., Klinger, Y., Amrat, A.Q., Agnon, A., Dorbath, L., Baer, G., Ruegg, J.C., Charade, O., Mayyas, O., 2008. Slip rate and locking depth from GPS profiles across the southern Dead Sea transform. J. Geophys. Res. 113, B11403. http://dx.doi.org/10.1029/2007JB005280.
Liotta, M., Martelli, M., 2012. Dissolved gases in brackish thermal waters: an improved analytical method. Geofluids 12, 236–244. http://dx.doi.org/10.1111/j.1468-8123.2012.00365.x.
Lyberis, N., Yürür, T., Chorowicz, J., Kasapoglu, E., Gündogdu, N., 1992. The East Anatolian fault: an oblique collisional belt. Tectonophysics 204, 1–15.
Mahmoud, Y., Masson, F., Meghraoui, M., Cakir, Z., Alchalbi, A., Yavasoglu, H., Yönlü, O., Daoud, M., Ergintav, S., Inan, S., 2013. Kinematic study at the junction of the East Anatolian fault and the Dead Sea fault from GPS measurements. J. Geodyn. 67, 30–39. http://dx.doi.org/10.1016/j.jog.2012.05.006.
Marty, B., Jambon, A., 1987. $C/^3He$ in volatile fluxes from the solid Earth: implications for carbon geodynamics. Earth Planet. Sci. Lett. 83, 16–26.
McClusky, S.C., Balassanian, S., Barka, A., Ergintav, S., Georgie, I., Gurkan, O., Hamburger, M., Hurst, K., Kahle, H., Kastens, K., Kekelidse, G., King, R., Kotzev, V., Lenk, O., Mahmout, S., Mishin, A., Nadaria, M., Ouzounis, A., Paradisissis, D., Peter, Y., Pirilepin, M., Reilinger, R.E., Sanli, I., Seeger, H., Teableb, A., Toksöz, N., Veis, V., 2000. Global positioning system constraints on plate kinematics and dynamics in the eastern Mediterranean Caucasus. J. Geophys. Res. 105, 5695–5719.
McClusky, S., Reilinger, R., Mahmoud, S., Sari, D.B., Tealeb, A., 2003. GPS constraints on Africa (Nubia) and Arabia plate motion. Geophys. J. Int. 155, 126–138.
McKenzie, D.P., 1972. Active tectonics of the Mediterranean region. Geophys. J. R. Astro. Soc. 30, 109–185.
Meghraoui, M., Gomez, F., Sbeinati, R., Woerd, J., Mouty, M., Darkal, A.N., Radwan, Y., Layyous, I., Al Najjar, H., Darawcheh, R., Hijazi, F., Al-Ghazzi, R., Barazangi, M., 2003. Evidence for 830 years of seismic quiescence from palaeoseismology, archaeoseismology and historical seismicity along the Dead Sea fault in Syria. Earth Planet. Sci. Lett. 210, 35–52.
Meghraoui, M., Bertrand, S., Karabacak, V., Ferry, M., Çakır, Z., Altunel, E., 2006. Active deformation at the junction between the East Anatolian fault, Dead Sea fault and Cyprus Arc (Hatay Province, South Turkey). Kinematic modeling from Tectonic and GPS data, AGU Fall Meeting 2006, San Francisco, CA, USA, 11–15 December 2006.
Meghraoui, M., Çakır, Z., Masson, F., Mahmood, Y., Ergintav, S., Alchalbi, A., Inan, S., Daoud, M., Yonlu, O., Altunel, E., 2011. Kinematic modelling at the triple junction between the Anatolian, Arabian, African plates (NW Syria and in SE Turkey). Geophys. Res. Abstr. 13, EGU2011–EGU12599.
Morrill, P.L., Gijs Kuenen, J., Johnson, O.J., Suzuki, S., Rietze, A., Sessions, A.L., Fogel, M.L., Nealson, K.H., 2013. Geochemistry and geobiology of a present-day serpentinization site in California: the Cedars. Geochim. Cosmochim. Acta 109, 222–240. http://dx.doi.org/10.1016/j.gca.2013.01.043.
Muehlberger, R.W., 1981. The splintering of the Dead Sea fault zone in Turkey. H. U. Yerbilimleri Bull. 8, 123–130.
Over, S., Kavak, K.S., Bellier, O., Özden, S., 2004. Is the Amik Basin (SE Turkey) a triple-junction area? Analyses of SPOT XS imagery and seismicity. Int. J. Remote Sens. 25 (19), 3857–3872. http://dx.doi.org/10.1080/01431160310001654437.
Ozyurt, N.N., 2008. Residence time distribution in the Kirkgoz karst springs (Antalya-Turkey) as a tool for contamination vulnerability assessment. Environ. Geol. 53 (7), 1571–1583. http://dx.doi.org/10.1007/s00254-007-0811-x.
Parks, M.M., Caliro, S., Chiodini, G., Pyle, D.M., Mather, T.A., Berlo, K., Edmonds, M., Biggs, J., Nomikou, P., Raptakis, C., 2013. Distinguishing contributions to diffuse CO_2 emissions in volcanic areas from magmatic degassing and thermal decarbonation using soil gas ^{222}Rn–$\delta^{13}C$ systematics: application to Santorini volcano, Greece. Earth Planet. Sci. Lett. 377–378, 180–190. http://dx.doi.org/10.1016/j.epsl.2013.06.046.
Pearson, F.J., Truesdell, A.H., 1978. Tritium in the waters of Yellowstone National Park. US Geological Survey Open-file Report. ,pp. 78–701.
Proskurowski, G., Lilley, M.D., Brown, T.A., 2004. Isotopic evidence of magmatism and seawater bicarbonate removal at the Endeavour hydrothermal system. Earth Planet. Sci. Lett. 225 (1–2), 53–61.
Proskurowski, G., Lilley, M.D., Kelley, D.S., Olson, E.J., 2006. Low temperature volatile production at the Lost City Hydrothermal Field, evidence from a hydrogen stable isotope geothermometer. Chem. Geol. 229, 331–343.
Quennell, A.M., 1958. The structural and geomorphic evolution of the Dead Sea rift. Q. J. Geol. Soc. Lond. 114, 1–24.
Reilinger, R., McClusky, S.C., Oral, M.B., King, W., Toksöz, M.N., 1997. Global positioning, system measurements of present-day crustal movements in the Arabia–Africa–Eurasia plate collision zone. J. Geophys. Res. 102, 9983–9999.
Reilinger, R., McClusky, S., Vernant, P., Lawrence, S., Ergintav, S., Cakmak, R., Ozener, H., Kadirov, F., Guliev, I., Stepanyan, R., Nadariya, M., Hahubia, G., Mahmoud, S., Sakr, K., Ar Rajehi, A., Paradissis, D., Al-Aydrus, A., Prilepin, M., Guseva, T., Evren, E., Dmitrotsa, A., Filikov, S.V., Gomez, F., Al-Ghazzi, R., Karam, G., 2006. GPS constraints on continental deformation in the Africa–Arabia–Eurasia continental collision zone and implications for the dynamics of plate interactions. J. Geophys. Res. 111 (B5), B05411.
Robertson, A.H.F., 2002. Overview of the genesis and emplacement of Mesozoic ophiolites in the Eastern Mediterranean Tethyan region. Lithos 65, 1–67.
Rojay, B., Heimann, A., Toprak, V., 2001. Neotectonic and volcanic characteristics of the Karasu fault zone (Anatolia, Turkey): the transition zone between the Dead Sea transform and the East Anatolian fault zone. Geodin. Acta 14, 197–212.
Sano, Y., Wakita, H., 1985. Geographical distribution of $^3He/^4He$ in Japan: implications for arc tectonics and incipient magmatism. J. Geophys. Res. 90, 8729–8741.
Sengör, A.M.C., Yilmaz, Y., 1981. Tethyan evolution of Turkey: a plate tectonic approach. Tectonophysics 75, 181–241.
Seyrek, A., Demir, T., Pringle, M.S., Yurtmen, S., Westaway, R.W.C., Beck, A., Rowbotham, G., 2007. Kinematics of the Amanos Fault, southern Turkey, from Ar/Ar dating of offset Pleistocene basalt flows: transpression between the African and Arabian plates. In: Cunningham, W.D., Mann, P. (Eds.), Tectonics of Strike–Slip Restraining and Releasing Bends. Geological Society London Special Publications 290, pp. 255–284.
Shimizu, A., Sumino, H., Nagao, K., Notsu, K., Mitropoulos, P., 2005. Variation in noble gas isotopic composition of gas samples from the Aegean arc. Greece. J. Volcanol. Geotherm. Res. 140, 321–339. http://dx.doi.org/10.1016/j.jvolgeores.2004.08.016.
Suda, K., Ueno, Y., Yoshizaki, M., Nakamura, H., Kurokawa, K., Nishiyama, E., Yoshino, K., Hongoh, Y., Kawachi, K., Omori, S., Yamada, K., Yoshida, N., Maruyama, S., 2014. Origin of methane in serpentinite-hosted hydrothermal systems: the CH_4–H_2–H_2O hydrogen isotope systematics of the Hakuba Happo hot spring. Earth Planet. Sci. Lett. 386, 112–125. http://dx.doi.org/10.1016/j.epsl.2013.11.001.
Tatar, O., Piper, J.D.A., Gürsoy, H., Heimann, A., Koçbulut, F., 2004. Neotectonic deformation in the transition zone between the Dead Sea Transform and the East Anatolian Fault Zone, southern Turkey: a palaeomagnetic study of the Karasu Rift volcanism. Tectonophysics 385, 17–43.
Taymaz, T., Eyidogan, H., Jackson, J., 1991. Source parameters of large earthquakes in the East Anatolian Fault Zone (Turkey). Geophys. J. Int. 106, 537–550.
Tekeli, O., Erendil, M., Whitechurch, H., 1983. The Kizildag ophiolite. Autochthons, Parautochtons and Ophiolites of the Eastern Taurus and Amanos Mountains 1983. Field Guidebook, pp. 22–32.
Tezel, T., Shibutani, T., Kaypak, B., 2013. Crustal thickness of Turkey determined by receiver function. J. Asian Earth Sci. 75, 36–45.
TGDM, 2014. Turkish General Directorate of Meteorology. http://www.meteoroloji.gov.tr/veridegerlendirme/yillik-toplam-yagis-verileri.aspx?m=HATAY#sfB (accessed 07.05.2014).
Torfstein, A., Hammerschmidt, K., Friedrichsen, H., Starinsky, A., Garfunkel, Z., Kolodny, Y., 2013. Helium isotopes in Dead Sea transform waters. Chem. Geol. 352, 188–201. http://dx.doi.org/10.1016/j.chemgeo.2013.06.008.
Umeda, K., Ninomiya, A., McCrank, G.F., 2008. High ^3He emanations from the source regions of recent large earthquakes, central Japan. Geochem. Geophys. Geosyst. 9, Q12003. http://dx.doi.org/10.1029/2008GC002272.
Vanacore, E.A., Taymaz, T., Saygin, E., 2013. Moho structure of the Anatolian Plate from receiver function analysis. Geophys. J. Int. 193, 329–337. http://dx.doi.org/10.1093/gji/ggs107.
Wdowinski, S., Bock, Y., Baer, G., Prawirodirdjo, L., Bechor, N., Naaman, S., Knafo, R., Forrai, Y., Melzer, Y., 2004. GPS measurements of current crustal movements along the Dead Sea Fault. J. Geophys. Res. 109 (B5), 5403.

Westaway, R., 1994. Present day kinematics of the Middle East and Eastern Mediterranean. J. Geophys. Res. 99, 12071–12090.
Westaway, R., 2004. Kinematic consistency between the Dead Sea fault zone and the Neogene and Quaternary left-lateral faulting in SE Turkey. Tectonophysics 391, 203–237.
Yilmaz, Y., Yifgitba, E., Gen, C., 1993. Ophiolitic and metamorphic assemblages of south-east Anatolia and their significance in the geological evolution of the orogenic belt. Tectonics 12 (5), 1280–1297.
Yuce, G., 1999. Karst hydrogeology of Yenisehir and Cudeyde (Hatay-Reyhanlı, Turkey) springs. DSI Project Report, No. 49. , (in Turkish).
Yuce, G., 2001. Hydrogeologic characteristics of Hatay–Erzin plain and Burnaz spring. Geol. Eng. J. 25 (2), 21–46 (in Turkish).
Yuce, G., 2005. Determination of the recharge area and salinization degree of karst springs in the Lamas Basin (Turkey). Isot. Environ. Health Stud. 41 (4), 391–404.
Yuce, G., 2007. Discharge hydrodynamics of Yenisehir and Cudeyde (Reyhanli — Hatay) karst springs and hydrogeochemical properties. Journal of Architecture. 1301-045X vol. 20, no. 2. Engineering Faculty of Eskisehir Osmangazi University, pp. 159–187 (in Turkish).
Yuce, G., Demirkol, C., 1990. Groundwater Potential in the Lamas Karst Basin (Limonlu–Erdemli/Turkey). Journal of Faculty of Engineering and Architecture Vol. 5, No. 1. Publications of Cukurova University, Turkey, pp. 91–117 (in Turkish).
Yurtmen, S., Guillou, H., Westaway, R., Rowbotham, G., Tatar, O., 2002. Rate of strike–slip motion on the Amanos fault (Karasu Valley, southern Turkey) constrained by K–Ar dating and geochemical analysis of Quaternary basalts. Tectonophysics 344, 207–246.
Yürür, T., Chorowicz, J., 1998. Recent volcanism, tectonics and plate kinematics near the junction of the African, Arabian and Anatolian plates in the eastern Mediterranean. J. Volcanol. Geotherm. Res. 85, 1–15.
Ziegler, M.A., 2001. Late Permian to Holocene Paleofacies evolution of the Arabian plate and its hydrocarbon occurrences. GeoArabia 6, 445–504.